

# Dwarf Nova Outbursts with Magnetorotational Turbulence

M. S. B. Coleman<sup>1\*</sup>, I. Kotko<sup>2†</sup>, O. Blaes<sup>1</sup>, J.-P. Lasota<sup>2,3</sup>, and S. Hirose<sup>4</sup>

<sup>1</sup> *Department of Physics, University of California, Santa Barbara, CA 93106, USA*

<sup>2</sup> *Nicolaus Copernicus Astronomical Center, Polish Academy of Sciences, Bartycka 18, 00-716 Warszawa, Poland*

<sup>3</sup> *Institut d'Astrophysique de Paris, CNRS et Sorbonne Universités, UPMC Univ Paris 06, UMR 7095, 98bis Bd Arago, 75014 Paris, France*

<sup>4</sup> *Department of Mathematical Science and Advanced Technology, Japan Agency for Marine-Earth Science and Technology, Yokohama, Kanagawa 236-0001, Japan*

Accepted —. Received —; in original form —

## ABSTRACT

The phenomenological Disc Instability Model has been successful in reproducing the observed light curves of dwarf nova outbursts by invoking an enhanced Shakura-Sunyaev  $\alpha$  parameter  $\sim 0.1 - 0.2$  in outburst compared to a low value  $\sim 0.01$  in quiescence. Recent thermodynamically consistent simulations of magnetorotational (MRI) turbulence with appropriate opacities and equation of state for dwarf nova accretion discs have found that thermal convection enhances  $\alpha$  in discs in outburst, but only near the hydrogen ionization transition. At higher temperatures, convection no longer exists and  $\alpha$  returns to the low value comparable to that in quiescence. In order to check whether this enhancement near the hydrogen ionization transition is sufficient to reproduce observed light curves, we incorporate this MRI-based variation in  $\alpha$  into the Disc Instability Model, as well as simulation-based models of turbulent dissipation and convective transport. These MRI-based models can successfully reproduce observed outburst and quiescence durations, as well as outburst amplitudes, albeit with different parameters from the standard Disc Instability Models. The MRI-based model lightcurves exhibit reflares in the decay from outburst, which are not generally observed in dwarf novae. However, we highlight the problematic aspects of the quiescence physics in the Disc Instability Model and MRI simulations that are responsible for this behavior.

**Key words:** accretion, accretion discs — MHD — turbulence — stars: dwarf novae.

## 1 INTRODUCTION

Dwarf novae are transient optical outbursts observed from close binary systems containing an accreting white dwarf. These outbursts have amplitudes up to  $\sim 8$  mag and last 2–20 days, with recurrence times ranging from  $\sim 4$  days to years (Lasota 2001). The Disc Instability Model (hereafter DIM) is a well-tested model that attributes the outbursts to a thermal-viscous<sup>1</sup> instability that arises at temperatures where hydrogen is ionizing in the accretion disc. During quiescence, a cold dwarf nova disc accumulates matter and heats until somewhere the temperature crosses a critical value which triggers the thermal instability. This creates heating fronts which propagate into the low-temperature zones, leaving behind ionized regions. In these hot regions of

the disc, the turbulence and the Shakura & Sunyaev (1973)  $\alpha$  parameter are assumed to be enhanced, leading to an increase in angular momentum transport. This causes mass, which during quiescence had gathered mostly in the outer parts of the disc, to diffuse inwards at a high rate. The DIM is also successful in explaining soft X-ray transient outbursts observed in close binary systems containing accreting neutron stars and black holes, although X-ray irradiation of the outer disc modifies the stability criterion (van Paradijs 1996) and plays an important role in extending the duration of the outburst in these systems (King & Ritter 1998; Dubus et al. 2001).

In addition to their intrinsic interest, the observed amplitudes and time scales present in dwarf nova light curves provide the best quantitative measurements of the stresses responsible for angular momentum transport in accretion discs (King et al. 2007). It was realized early on (e.g. Mineshige & Osaki 1983; Smak 1984; Meyer & Meyer-Hofmeister 1984) that the observed outburst amplitudes can only be reproduced in the DIM if the stress parameter  $\alpha$  takes on different values in the outburst (denoted by  $h$  for

\* E-mail: mcoleman@physics.ucsb.edu

† Now at the Pennsylvania State University, 222A Computer Building, University Park, PA 16802, USA

<sup>1</sup> To be clear, “viscosity” here and throughout the paper is an effective turbulent viscosity as opposed to a true molecular viscosity.

hot) and quiescent (denoted by  $c$  for cold) states, with  $\alpha_h$  being larger than  $\alpha_c$  by about a factor of ten. Modern versions of the DIM use an interpolation scheme between constant values of  $\alpha_h$  and  $\alpha_c$  in the outburst and quiescent states, but this does not imply that  $\alpha$  is necessarily constant for all high or for all low temperatures<sup>2</sup>. Detailed fits of the DIM to the observed correlations between orbital period (or, equivalently, outer disc radius) and the outburst duration and decay rate in normal, U Gem-type systems and normal outbursts of SU UMa systems, give values for  $\alpha_h$  of between 0.1 and 0.2, and certainly rule out significantly smaller values (Smak 1999; Kotko & Lasota 2012). Moreover, only such high values are able to explain the observed linear relationship between outburst amplitude and the logarithm of outburst recurrence time (the Kukarkin-Parenago relation; Kotko & Lasota 2012).

Ever since the first application of the magnetorotational instability (MRI) to accretion discs (Balbus & Hawley 1991; Hawley & Balbus 1991), it has been widely suspected that both angular momentum transport and dissipation of mechanical energy is mediated by MRI turbulence, at least if the disc is sufficiently electrically conducting. The accretion stress is due to correlations between radial and azimuthal magnetic field fluctuations, as well as radial and azimuthal velocity fluctuations (e.g. Balbus & Hawley 1998). One can measure this stress directly from numerical simulations of the turbulence. Equivalent values of the  $\alpha$  parameter can then be derived by scaling this stress with the average thermal pressure.

Because the values of  $\alpha$  are among the most fundamental ways of confronting MRI turbulence with observations, many groups have measured these values from their simulations. In the absence of net vertical magnetic flux, local shearing box simulations that incorporate vertical gravity generally give time-averaged  $\alpha$  values of around two or three percent (Hirose et al. 2006; Davis et al. 2010; Shi et al. 2010; Guan & Gammie 2011; Simon et al. 2012). Global simulations without net vertical flux of the entire disc, but which allow for large scale field loops that can produce local vertical magnetic fluxes threading the disc, also so far produce comparably small values of  $\alpha$  (Sorathia et al. 2010; Hawley et al. 2011; Sorathia et al. 2012), though more work needs to be done in exploring the effects of various field topologies.

A number of suggestions have been made as to how to resolve the discrepancy between the high values of  $\alpha$  inferred from dwarf novae in outburst, and these low values measured in MRI simulations. First, it has been known for some time that shearing box simulations with no vertical gravity have stronger  $\alpha$  values when the box is threaded by a vertical magnetic field, and the resulting  $\alpha$  increases with magnetic field strength so long as the critical vertical wavelength of the MRI lies within the box (Hawley et al. 1995; Sano et al. 2004; Pessah et al. 2007).<sup>3</sup> Because the initial total vertical magnetic flux is necessarily conserved in shearing box simulations, this would appear to require imposing a net external

vertical magnetic field in the disc from the outside in order to increase the value of  $\alpha$  in outburst states. This might result from the magnetic field of the companion star, although one would then have to explain why the resulting value of  $\alpha$  is so universal in the outburst state.

On the other hand, the increase in local stress with *local* vertical magnetic flux has been confirmed in global simulations with no overall net vertical magnetic flux, although the global disc still has a low value of  $\alpha$  when averaged over the entire disc (Sorathia et al. 2010). Having net vertical flux may also drive magnetocentrifugal winds, which can also extract angular momentum from the disc (Suzuki & Inutsuka 2009; Fromang et al. 2013; Lesur et al. 2013; Bai & Stone 2013). In addition to the vertical magnetic field, transient phases such as those caused by the dwarf nova outbursts themselves may also produce periods of enhanced  $\alpha$  that are similar to that observed in transient magnetic field growth phases in global simulations (Sorathia et al. 2012).

Even without vertical magnetic field or transient behavior, however, radiation MHD stratified shearing box simulations that incorporate a realistic equation of state and opacities near the hydrogen ionization transition reproduce thermal equilibria resembling the stable upper and lower branches of the local “S-curve” of the DIM (Hirose et al. 2014). As in previous MRI simulations,  $\alpha$  values of a few percent generally result, but  $\alpha$  dramatically increases as one approaches the lower end of the upper branch. This appears to be due to the onset of intermittent vertical convection caused by the large increase in opacity near the ionization transition. The resulting vertical motions at the beginning of the convective episodes build up vertical magnetic field, which may be seeding the axisymmetric MRI. In addition, temporal phase differences between the variations of stress and pressure may also be increasing the time-averaged  $\alpha$ .<sup>4</sup> These simulations therefore reproduce the observed high values of  $\alpha$  on the upper branch of the S-curve, but only near the low-temperature end of the upper branch.

In addition to the variations of  $\alpha$  on the upper branch, there are significant differences in the time-averaged vertical structure observed in the simulations and the standard assumptions used in the DIM. First, the DIM generally assumes that the stress to pressure ratio is constant with height, so that the dissipation rate per unit volume is proportional to pressure. MRI simulations, on the other hand, generally produce a more extended vertical dissipation profile (Turner 2004; Hirose et al. 2006). Moreover, the simulated upper, near-photosphere layers are generally supported against the vertical tidal gravity by magnetic forces, not thermal pressure forces (Miller & Stone 2000; Hirose et al. 2006), in contrast to the DIM vertical structure models. Finally, as we have just discussed, vertical transport of heat in the simulations is caused by alternating episodes of radiative diffusion and thermal convection, at least near the end of the upper branch. The DIM incorporates the possibility of convection using mixing length theory, but it is not clear that this prescription adequately describes what is happening in the MRI simulations.

The primary purpose of this paper is to incorporate the

<sup>2</sup> E.g. Mineshige & Wheeler (1989) used  $\alpha \sim (H/R)^{1.5}$ .

<sup>3</sup> Recent work by Shi et al. (2016) has also shown that the value of  $\alpha$  in shearing boxes with no vertical magnetic field or vertical gravity is sensitive to the height of the box: taller boxes produce significantly higher values of  $\alpha$ .

<sup>4</sup> Persistent convection can also enhance  $\alpha$ , provided the Mach numbers of the convective motions exceed  $\sim 0.01$  (Hirose 2015).

variation of  $\alpha$  measured in the MRI simulations into the DIM, to see whether an enhancement of  $\alpha$  just near the end of the upper branch is sufficient to reproduce the observed amplitudes and time scales in dwarf nova outburst light curves. A secondary objective is to use the dissipation and heat transport observed in the simulations to produce more physics-based vertical structure models that can be incorporated in the DIM. In section 2, we discuss the behavior of the  $\alpha$  parameter in the MRI simulations, including new simulations done at different radii in the disc from those originally done by Hirose et al. (2014). It turns out that  $\alpha$  can be reasonably fit by a function of just local disc effective temperature. In section 3 we present time-averaged vertical dissipation profiles from the simulations, and show how these can be incorporated into the DIM vertical model equations. We also briefly discuss the evolution of MRI simulations when they are not in thermal equilibrium, and show how this evolution is surprisingly consistent with the standard effective  $\alpha$  prescription currently used in the DIM. Finally, we also present a mixing length prescription which appears able to reproduce the time-averaged vertical structures observed in the simulations on the upper branch. In section 4, we present theoretical dwarf nova outburst light curves using these MRI simulation-based prescriptions, and compare them to the standard DIM light curves. We discuss our results in section 5, and summarize our conclusions in section 6.

## 2 MRI SIMULATION-BASED STRESS PRESCRIPTION

As discussed in the introduction, the ratio of vertically averaged stress to vertically averaged thermal pressure,  $\alpha$ , can be inferred from observations and can be measured directly from simulations. The difference in  $\alpha$  between the lower and upper branches of the S-curve has been crucial for getting DIMs to produce realistic light curves. In the standard version of the DIM two values of  $\alpha$  were used;  $\alpha_h \sim 0.1$  for the hot, ionized upper branch, and  $\alpha_c$ , 4 to 10 times smaller, for the lower branch, with some smooth and rapid transition between them. In particular, our modeling of the standard DIM here in this paper will use a slightly modified version of the prescription first introduced by Hameury et al. (1998):

$$\log(\alpha) = \log(\alpha_c) + [\log(\alpha_h) - \log(\alpha_c)] \left[ 1 + \left( \frac{T_{c0}}{T_c} \right)^{16} \right]^{-1}, \quad (1)$$

where  $T_c$  is the central (midplane) temperature and  $T_{c0}$  is a critical temperature. The choice of this parameter is somewhat arbitrary and we take  $T_{c0} = 2.9 \times 10^4$  K (Lasota et al. 2008), and take the limiting  $\alpha$ -parameters to be  $\alpha_c = 0.03$  and  $\alpha_h = 0.12$ .

Until recently, local shearing box MRI simulations (without net vertical flux through the simulation domain) produced values of  $\alpha$  which are too low for the hot ionized outburst state of dwarf novae. However, for the first time,  $\alpha$  measured in local MRI simulations (Hirose et al. 2014) appear to be consistent with  $\alpha$  values inferred from observations and commonly used to reproduce dwarf novae outbursts by the DIM. Hirose et al. (2014) found that the  $\alpha$  parameter varies along the S-curve and is not constant on

the upper branch, with an enhancement of  $\alpha$  towards the tip (low temperature end) of the upper branch. This provides an intriguing replacement for the previous ad hoc bimodal  $\alpha$  prescription previously used (e.g. Hameury et al. 1998; Lasota 2001; Kotko & Lasota 2012).

The Hirose et al. (2014) simulations are done in the geometry of a vertically stratified shearing box, in which a small local patch of an accretion disc is approximated as a co-rotating Cartesian frame  $(x, y, z)$  with linearized Keplerian shear flow  $-(3/2)\Omega x$ , where  $x$ ,  $y$ , and  $z$  correspond to the radial, azimuthal, and vertical coordinates, respectively (Hawley et al. 1995). The simulations assume no explicit shear viscosity in the basic equations, and no Ohmic, Hall, or ambipolar diffusion effects are included either, i.e. ideal MHD is assumed. The simulations are therefore probably not accurate for the quiescent, largely electrically neutral state where Ohmic dissipation and the Hall effect are likely important (see Appendix A). Magnetic and kinetic energy losses at the grid scale are captured and added to the local internal energy of the gas, creating an effective turbulent dissipation (Turner et al. 2003; Hirose et al. 2006). Additionally, the simulations include realistic equation of state and opacity tables in order to accurately model the hydrogen ionization regime (see Hirose et al. 2014, for details), and the flux limited diffusion approximation (which breaks down at low optical depths) is used to model radiation transport and cooling.

The simulations in Hirose et al. (2014) were computed for only one angular frequency  $\Omega = 6.4 \times 10^{-3} \text{ s}^{-1}$ , which corresponds to a distance<sup>5</sup> of  $1.25 \times 10^{10}$  cm from a white dwarf of  $0.6 M_\odot$ . In order to explore a larger parameter space, we utilize the same methods to run simulations at two additional orbital radii,  $1.25 \times 10^9$  cm and  $4.13 \times 10^9$  cm. The parameters for these additional simulations can be found in Table B1.

We incorporate simulation data into the DIM's vertical thermal equilibrium equations (Hameury et al. 1998) by first discarding the initial 10 orbits of data (this is the time it take for turbulence to develop and erase details of the initial conditions) and taking a time average of the remaining duration of the simulations. All the simulations have been run long enough so that at least 100 orbits (and up to 220 orbits) of data are included in the time averaging. This ensures that averaging is done over many thermal times so that thermal fluctuations are smoothed out and that the average is well behaved (i.e. running the simulation for another 10 orbits would have little effect on the time average). We also horizontally average the data over the radial ( $x$ ) and azimuthal ( $y$ ) directions. Finally, we vertically symmetrize the data about the midplane  $z = 0$ . Simulation data which have undergone these operations will henceforth be referred to as profiles. To summarize, for some scalar data  $f$  the profile is calculated as follows

$$f(z) \equiv \frac{\iiint [f(x, y, z, t) + f(x, y, -z, t)] dx dy dt}{2 \iiint dx dy dt}. \quad (2)$$

We then fit some of these profiles in order to produce vertical structures that more accurately represent simulation physics than the standard DIM.

<sup>5</sup> Due to some rounding differences our distance slightly differs from the  $1.23 \times 10^{10}$  cm that Hirose et al. (2014) state.

The parameter  $\alpha$  is computed from each simulation as follows

$$\alpha \equiv \frac{\int w_{xy}(z) dz}{\int [P_{\text{gas}}(z) + P_{\text{rad}}(z)] dz}, \quad (3)$$

where  $w_{xy}$  is the sum of the Maxwell and Reynolds stresses

$$w_{xy} \equiv -\frac{B_x B_y}{4\pi} + \rho v_x \delta v_y. \quad (4)$$

Here  $B_x$  and  $B_y$  are the radial and azimuthal components of the magnetic field respectively<sup>6</sup>,  $v_x$  is the radial velocity, and  $\delta v_y \equiv v_y + 3\Omega x/2$  is the difference between the azimuthal velocity and the mean rotational velocity in the disc. We also examined how the temporal mean of  $\alpha$  varies with time and we found these fluctuations diminished with time, indicating that the time averaged  $\alpha$  is well behaved. Provided the time average is done over an interval of at least 100 orbits, differences in the time-averaged value of  $\alpha$  within a single simulation are less than ten percent.

We fit the variation of  $\alpha$  between all the simulations at radius  $r = 1.25 \times 10^{10}$  cm with a prescription depending only on local effective temperature  $T_{\text{eff}}$  of the following form

$$\alpha = a \exp\left(-\frac{x^2}{2}\right) + \frac{b}{2} \tanh(x) + c, \quad (5)$$

$$x = \frac{T_{\text{eff}} - T_0}{\sigma}. \quad (6)$$

The best fit parameter values are  $a = 8.79 \times 10^{-2}$ ,  $b = 2.41 \times 10^{-3}$ ,  $c = 3.27 \times 10^{-2}$ ,  $T_0 = 7034$  K, and  $\sigma = 1000$  K. Figure 1 compares this fit to the simulation data at this radius. Also shown are the results from simulations at two additional radii (which are not included in the fit), which are also reasonably consistent with this fit, though there is some indication that the simulations at smaller radii have slightly greater convective enhancements of  $\alpha$ . We will use the fit of equations (5) and (6) in the simulation-based light curve modeling below.

### 3 MRI SIMULATION-BASED VERTICAL STRUCTURE MODELS

In addition to the overall behavior of the stress to pressure ratio  $\alpha$  discussed in the previous section, MRI simulations also exhibit differences with the standard DIM assumptions concerning the local vertical structure of the disc. Here we utilize data from the Hirose et al. (2014) vertically stratified shearing box MHD simulations to show how to make DIM vertical structure models that better reflect some of the actual properties of the turbulence observed in the simulations.

#### 3.1 Dissipation Profile

Previously the DIM has relied on an ad hoc assumed vertical profile of turbulent dissipation, in particular a *vertically local*  $\alpha$  prescription in which the dissipation rate per unit volume

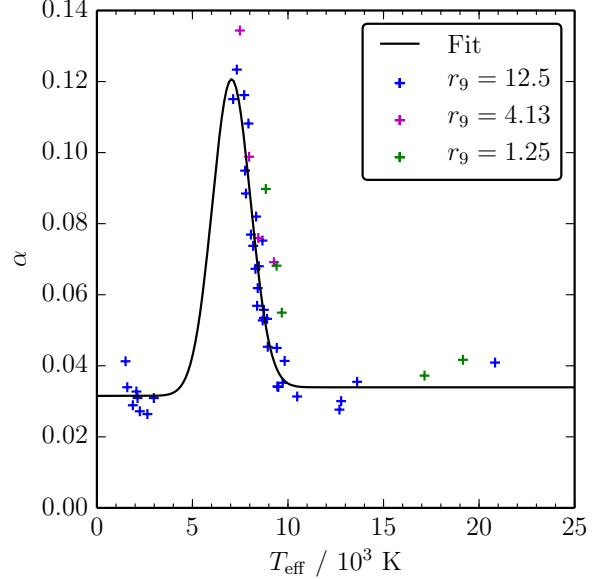


**Figure 1.** Time averaged  $\alpha$  versus effective temperature for all the MRI simulations at three different radii around a  $0.6M_{\odot}$  white dwarf:  $r = 1.25 \times 10^{10}$  cm (blue crosses),  $r = 4.13 \times 10^9$  cm (magenta crosses), and  $r = 1.25 \times 10^9$  cm (green crosses). The best fit curve for the  $r = 1.25 \times 10^{10}$  cm simulations is plotted in black.

is proportional to the local thermal pressure. This is very different from what is observed in vertically stratified MRI simulations. Such simulations of course cannot spatially resolve the actual microscopic viscous and resistive length scales in the plasma, and the simulations of Hirose et al. (2014) do not include any explicit resistivity or shear viscosity in the basic equations. Instead, a total energy scheme is employed in which grid scale losses of magnetic and kinetic energy are automatically transferred to internal energy of the plasma, thereby effecting a dissipation of turbulent mechanical energy. This will capture the true dissipation rate in the turbulence provided the turbulent cascade that would exist in reality below the grid scale is capable of transferring most of the energy down to the true microscopic dissipation scales. Whether this accurately captures the dissipation occurring in real discs in nature remains to be seen.

In fact, there is strong numerical evidence that the saturation level of the turbulent stresses, and even whether long-lived turbulence can be maintained, depends on the values of the fluid and magnetic Reynolds numbers or their ratio, the magnetic Prandtl number. This is particularly true of shearing box simulations that lack vertical gravity (e.g. Fromang et al. 2007; Lesur & Longaretti 2007). Including vertical gravity appears to slightly extend the range of magnetic Prandtl numbers that allow sustained turbulence to lower (but still greater than unity) values (Davis et al. 2010). This is also true of shearing box simulations which lack vertical gravity, provided the box height is large enough (Shi et al. 2016). Because the simulations used here have no explicit viscosity or resistivity, and dissipation effectively occurs at the grid scale, the effective magnetic Prandtl number must be of order unity. While the simulations nevertheless exhibit sustained turbulence, more work needs to be done

<sup>6</sup> Note that the magnetic fields as defined here differ by a factor of  $\sqrt{4\pi}$  from the magnetic fields defined in the simulations. Here we use standard cgs Gaussian units.

to investigate whether and how the dissipation profiles, and even the saturation level of the turbulence, might be affected by the actual dissipation scales. Dependencies of the turbulent stresses on magnetic Prandtl number may even themselves lead to thermal instabilities in accretion discs (Potter & Balbus 2014).

In any case, as shown in Figure 2, the time and horizontally-averaged vertical profile of dissipation rate per unit volume in the simulations is not proportional to the pressure, in contrast to the simple assumption used in the DIM. In fact, the vertical dissipation profile generally does not even decline monotonically away from the midplane, but instead peaks off the midplane, possibly due to the effects of magnetic buoyancy (Blaes et al. 2011). Despite this non-monotonic behavior, we find that we can adequately replace the usual DIM assumption of dissipation rate per unit volume  $Q^+$  being simply proportional to thermal pressure with, instead, a power law dependence on thermal pressure (see Figure 2):

$$\frac{Q^+}{Q_0^+} = \left( \frac{P}{P_0} \right)^\delta, \quad (7)$$

where the subscript zero is used to denote midplane values. By thermal pressure  $P$ , we mean the sum of gas pressure ( $P_{\text{gas}}$ ) and the much smaller radiation pressure ( $P_{\text{rad}} \ll P_{\text{gas}}$ ), but we exclude magnetic pressure, which typically dominates the thermal pressure far from the midplane. Using linear regression (in log space) we determined that the best fit exponent  $\delta = 0.35$ . The ratio  $Q_0^+/P_0^\delta$  is chosen such that the vertically integrated Shakura & Sunyaev (1973)  $\alpha$  relation holds:

$$\frac{3}{2} \alpha \Omega \int_{-\infty}^{\infty} P(z) dz = \int_{-\infty}^{\infty} Q^+(z) dz. \quad (8)$$

### 3.2 Non-Equilibrium Dissipation

During the passage of a heating or cooling front through the disc, annuli at the location of the fronts are of course out of thermal equilibrium. Within the DIM (Hameury et al. 1998), this is handled by constructing hydrostatic vertical structures with a local vertical energy flux divergence given by

$$\frac{dF_z}{dz} = \frac{3}{2} \alpha_{\text{eff}} \Omega P(z), \quad (9)$$

where  $P(z)$  is the local thermal pressure and  $\alpha_{\text{eff}}$  is a parameter that differs from  $\alpha$  when the annulus is not in thermal equilibrium, both because vertically integrated heating and cooling will then no longer be equal and because of the concomitant vertical thermal expansion or contraction. The actual value that  $\alpha_{\text{eff}}$  takes is determined by solving for the complete vertical structure for a given effective temperature and surface mass density. If thermal equilibrium does hold, then  $\alpha_{\text{eff}} = \alpha$ , and we recover the standard DIM assumption that the dissipation rate per unit volume is proportional to the local thermal pressure at every height in the annulus.

As just noted, the time and horizontally averaged vertical profiles of dissipation rate per unit volume measured in the MRI simulations do not simply scale with local thermal pressure. We therefore modify equation (9) to be consistent with our fit to the equilibrium dissipation profile,

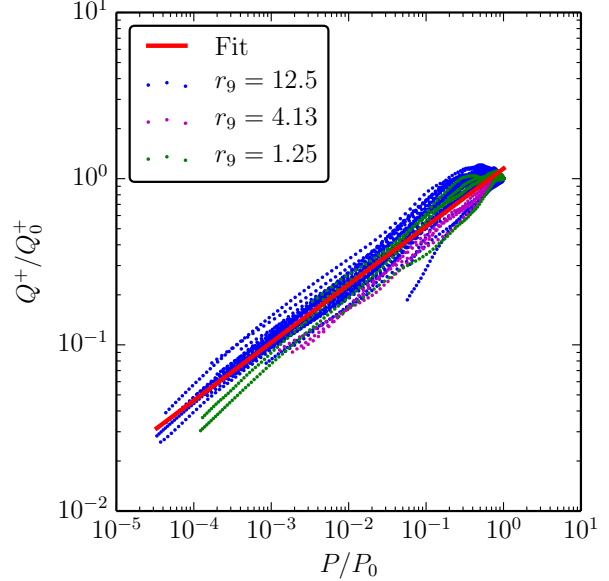


**Figure 2.** Time and horizontally averaged profiles of dissipation rate per unit volume as a function of thermal pressure, each scaled by their respective midplane values, for each of the MRI simulations used in this paper. The different colors refer to simulations done at three different radii around a  $0.6M_\odot$  white dwarf:  $r = 1.25 \times 10^{10}$  cm (blue points),  $r = 4.13 \times 10^9$  cm (magenta points), and  $r = 1.25 \times 10^9$  cm (green points). A power law fit to the profiles is also plotted (red line). Note that the slope of the fit is significantly more important than the vertical offset, which we determine in our light curve modeling by enforcing energy conservation using equation (8).

equation (7):

$$\frac{dF_z}{dz} = \frac{3}{2} \alpha_{\text{eff}} \Omega P_0 \left( \frac{P(z)}{P_0} \right)^\delta. \quad (10)$$

However, it is not obvious that the MRI simulations should behave according to this equation outside thermal equilibrium.

If the assumption of equation (10) were perfect, then all simulation data would fall directly on the best-fit line in Figure 2. While time averaged profiles lie near this line, it is not apparent that one should expect this behavior from a thermally evolving simulation. To test this we defined

$$\alpha_{\text{eff}}(z, t) \equiv \frac{2}{3} \frac{1}{\Omega P_0} \frac{\partial F_z}{\partial z} \left( \frac{P_0}{P} \right)^\delta, \quad (11)$$

with  $\delta = 0.35$  as previously discussed, and examined variations in  $\alpha_{\text{eff}}$  for a few simulations (see Figures 3-5). In addition to stable simulations (e.g. ws0446 shown in Figure 3), we specifically examined two non-equilibrium simulations: one heating (ws0467, see Figure 4), and one cooling (ws0488, see Figure 5). These simulations were started just beyond the edges of the lower and upper branches of the S-curve, respectively (see Figure 11 of Hirose et al. 2014). As these two simulations evolve, they move around on the plane of  $T_{\text{eff}}$  vs. total column mass density  $\Sigma$ , which allows  $\alpha_{\text{eff}}$  to vary with time. However,  $\alpha_{\text{eff}}$  should be approximately constant in height at a given time if equation (10)

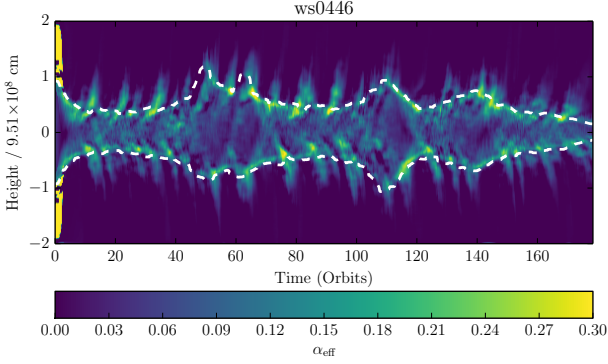


**Figure 3.** Horizontally averaged  $\alpha_{\text{eff}}$  for simulation ws0446, a stable convective simulation. The horizontal axis is time in orbits, and the vertical axis is height. The white dashed contours are the photospheres. The data has been smoothed with a two orbit running boxcar.

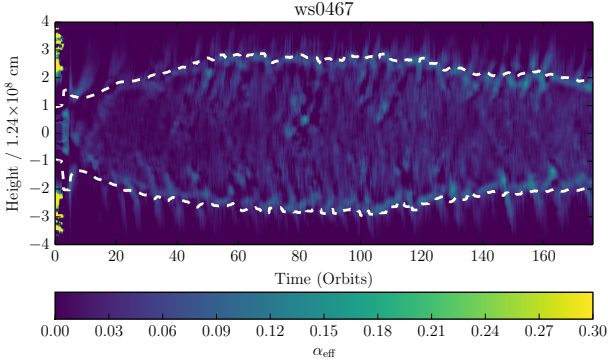


**Figure 4.** Horizontally averaged  $\alpha_{\text{eff}}$  for simulation ws0467, an unstable simulation that undergoes runaway heating until significant mass loss occurs through the vertical boundaries. The horizontal axis is time in orbits, and the vertical axis is height. The white dashed contours are the photospheres. The data has also undergone two orbit boxcar smoothing. This simulation exhibits continuous convective vertical transport of heat.

is to adequately describe the simulation behavior. With the exception of variations near and outside the photospheres, this seems to be a reasonable approximation for simulations ws0446 and ws0467. There are some clear issues for the cooling simulation ws0488 just below the photosphere (see Figure 5), which manifest as asymmetric regions of enhanced  $\alpha_{\text{eff}}$ . It is possible that these regions arise from asymmetric cooling/collapsing of the disc, which is not possible to incorporate into the DIM and show a clear limitation of our strategy. However, outside these regions, ws0446 and ws0488 show comparable variations, signifying that this approach is not unreasonable.

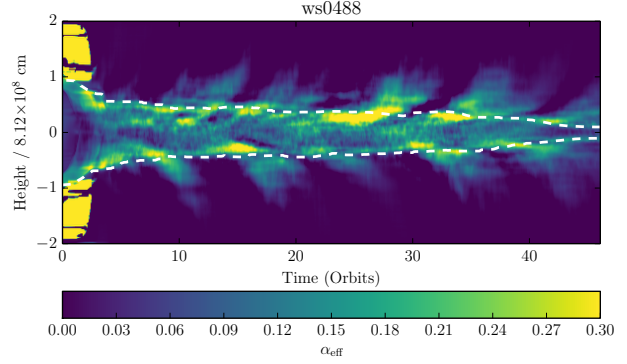


**Figure 5.** Horizontally averaged  $\alpha_{\text{eff}}$  for simulation ws0488, an unstable simulation that undergoes runaway cooling. The horizontal axis is time in orbits, and the vertical axis is height. The white dashed contours are the photospheres. The data has also undergone two orbit boxcar smoothing.

### 3.3 Mixing Length Theory

The vertical temperature profile is computed in the DIM according to

$$\nabla \equiv \frac{d \ln T}{d \ln P} = \begin{cases} \nabla_{\text{rad}} & \text{if } \nabla_{\text{rad}} \leq \nabla_{\text{ad}} \\ \nabla_{\text{conv}} & \text{if } \nabla_{\text{rad}} > \nabla_{\text{ad}} \end{cases} \quad (12)$$

$$\nabla_{\text{rad}} \equiv \frac{3\kappa\rho H_P F_{\text{tot}}}{16\sigma T^4}, \quad (13)$$

where  $\nabla_{\text{rad}}$  and  $\nabla_{\text{ad}}$  are the standard radiative and adiabatic temperature gradients, respectively,  $\nabla_{\text{conv}}$  is the convective temperature gradient computed using mixing length theory (Paczynski 1969; Hameury et al. 1998),  $\kappa$  is the Rosseland mean opacity,  $H_P$  is the pressure scale height, and  $F_{\text{tot}}$  is the total flux passing through a given height. Through trial and error we determined that using a value of six for the mixing length parameter ( $\alpha_{\text{ml}} = 6$ ) produced vertical structure models which closely resemble the time and horizontally averaged vertical profiles measured in the MRI simulations that exhibit convection (see Figure 6). This is compared to the much lower and more conventional value of 1.5 used in the DIM by Hameury et al. (1998). We note that if the mixing length theory is to be taken at face value then  $\alpha_{\text{ml}} = 6$  implies that the length scale of convective eddies is several ( $\sim 6$ ) times larger than the pressure scale height of the disc, which seems unphysical.

However, it is important to note that this value of the mixing length parameter actually reflects the fact that when convection occurs in the simulations, it does so *intermittently*. This intermittency is the result of a limit cycle, operating on timescales of  $\sim 10$  thermal times, which is driven by the interplay of temperature dependent opacities and enhancement of stress by convective turbulence (see Section 3.4 of Hirose et al. 2014, for further discussion). Averaging over this time dependent cycle results in a high effective  $\alpha_{\text{ml}}$ , but the time dependent  $\alpha_{\text{ml}}$  tend to have more canonical values of  $\sim 1$  when convection is occurring. By measuring the horizontally-averaged convective heat flux  $F_{\text{conv}}$  directly from the simulations, we compute the mixing length parameter  $\alpha_{\text{ml}}$  that would produce this flux as a function of height and time. We accomplished this by solving the following



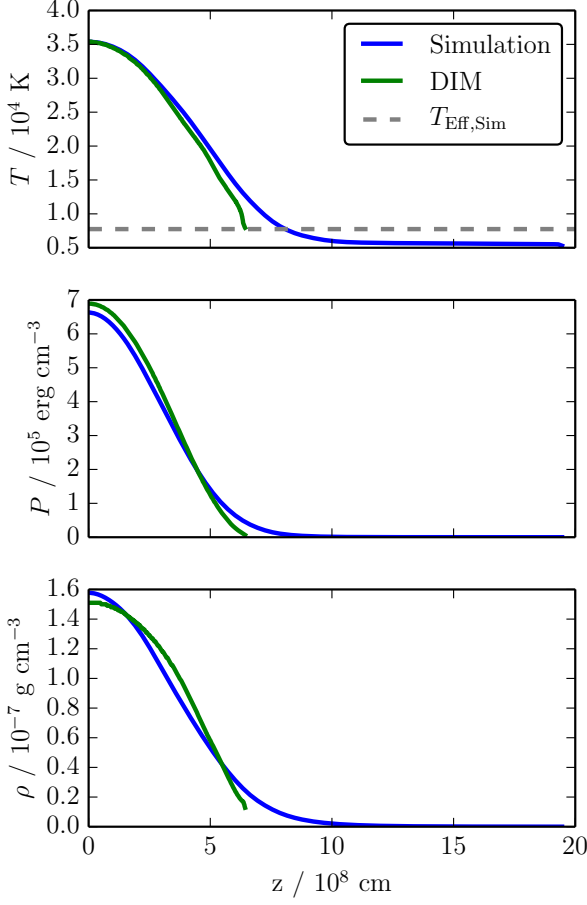


**Figure 6.** Comparison of vertical structure model to a convective simulation (ws0441) with  $r = 1.25 \times 10^{10}$  cm. Profiles of temperature (top), thermal pressure (middle), and mass density (bottom) are plotted versus  $z$  for profiles measured from the simulation (blue) and vertical structure models (green). In these plots, it is clear that the simulations extend further than our models. This is because our DIM vertical structures use the photosphere as a vertical boundary condition and thus terminate there. Thus the minimum temperature in the vertical structure model is also the effective temperature. The time averaged effective temperature of the simulation is plotted as the dashed gray horizontal line. Thus this figure clearly shows good agreement between our modified DIM and the simulations.

equations using the Newton-Raphson method:

$$\alpha_{\text{ml}}^2 \beta^{3/2} = \frac{2F_{\text{conv}}}{C_P \rho u T}, \quad (14)$$

where

$$u \equiv \sqrt{-\frac{g_z H_P}{8} \left( \frac{\partial \ln \rho}{\partial \ln T} \right)_P}, \quad (15)$$

$$H_P \equiv -\text{sign}(z) \frac{\partial z}{\partial \ln P}, \quad (16)$$

$\beta \equiv (\nabla - \nabla')$  is the positive root of the quadratic

$$\beta = (\gamma_0 \alpha u)^2 (\nabla - \nabla_{\text{ad}} - \beta)^2, \quad (17)$$

and

$$\gamma_0 \equiv \frac{C_P \rho}{8 \sigma T^3 \theta}, \quad \theta \equiv \frac{3\tau}{3 + \tau^2}, \quad \tau \equiv \alpha_{\text{ml}} \kappa \rho H_P. \quad (18)$$

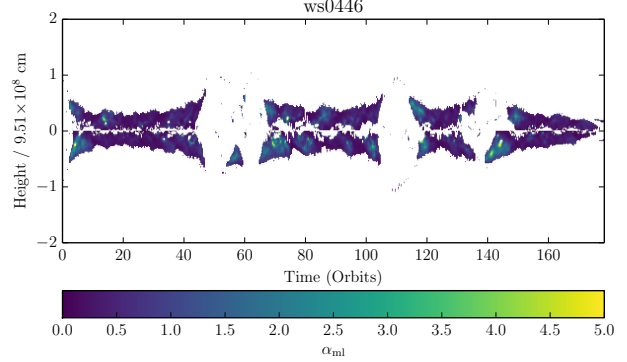


**Figure 7.** Convective mixing length parameter  $\alpha_{\text{ml}}$  computed locally from horizontally-averaged simulation data for upper branch simulation ws0446 from Hirose et al. (2014), as a function of height and time. The  $\alpha_{\text{ml}}$  data (already computed from quantities smoothed over 1 orbit) has been smoothed by an additional 0.2 orbits in time to improve clarity. White regions within two pressure scale heights are either convectively stable, or are regions for which our Newton-Raphson method to solve equations (14)-(18) failed to converge within 100 iterations. Data outside two pressure scale heights are discarded. The white gaps approximately centered on the 55 orbit, 110 orbit, and 140 orbit epochs are times when radiative diffusion dominated convection in the vertical transport of heat.

Note that  $\beta$  and  $\gamma_0$  are implicit functions of  $\alpha_{\text{ml}}$ .  $F_{\text{conv}}$ ,  $C_P$ ,  $\rho$ ,  $T$ ,  $g_z = -\Omega^2 z$ ,  $H_P$ ,  $\nabla$ ,  $\nabla_{\text{ad}}$ , and  $\kappa$  are read or computed from the MHD simulations. These variables are then horizontally averaged and smoothed by 1 orbit in time before  $\alpha_{\text{ml}}$  is computed.

The results are shown in Figure 7. The epochs that are white at all heights in this figure are epochs when radiative diffusion dominates, and there is little vertical convective transport of heat. Most of the epochs that are actually convective have very reasonable values of  $\alpha_{\text{ml}}$  that are of order unity. It is generally only near the epochs that are radiative that  $\alpha_{\text{ml}}$  takes on substantially larger values.

The vertical profiles of the simulation data shown in Figure 6 average over both the convective and radiative epochs, so it is not surprising, given the behavior shown in Figure 7, that unusually large mixing length parameters are required to describe these profiles with a pure convective transport treatment.

From the discussion here it is clear that time averaging the intermittent convection obscures some of the physics discovered in the MRI simulations of Hirose et al. (2014). It is unclear how much this simplification affects the outcome. The duration of the convective limit cycle is  $\sim 50$  orbits, so for timescales  $\gtrsim 1$  day, this averaging procedure should be a reasonable approximation. It is during the rapid transition from quiescence to outburst that this simplification becomes questionable, making the inability of the DIM to capture this time dependent behavior a clear limitation, but nothing better can be done in the framework of the standard DIM.

### 3.4 Summary of MRI Simulation-Based Vertical Structure Equations and Boundary Conditions

The DIM framework uses the thermal pressure to provide both the vertical hydrostatic support and to specify the vertical dissipation profile. In the simulations, magnetic pressure support can dominate thermal pressure near the photosphere, although the magnetic to thermal pressure ratio is at most  $1.5\alpha \lesssim 20\%$  near the midplane. Including magnetic pressure in a single pressure framework is complicated, as it requires a modification of the alpha relation (equation 8) and it complicates the temperature gradient (equation 12) used in mixing length theory. We have therefore neglected this additional aspect of the simulation physics. Additionally, the DIM uses different, albeit similar, equation of state and opacity tables.

With our modifications to the DIM our vertical structure equations become

$$\frac{dP}{dz} = -\rho\Omega^2 z \quad (19)$$

$$\frac{d\varsigma}{dz} = 2\rho \quad (20)$$

$$\frac{d \ln T}{d \ln P} = \nabla \quad (21)$$

$$\frac{dF_z}{dz} = Q^+ = A_0 \Omega P_0 \left( \frac{P}{P_0} \right)^\delta \quad (22)$$

$$A_0 = \frac{3}{2} \alpha \frac{P_0^{\delta-1} \int_0^\infty P dz}{\int_0^\infty P^\delta dz}, \quad (23)$$

where  $\varsigma(z)$  is the surface mass density between  $\pm z$ , and  $\nabla$  is determined by equation (12). Equations (22) and (23) are equivalent to our dissipation fit and the alpha relation (equations 7 and 8, respectively). Our midplane boundary conditions are

$$z = 0 \quad (24)$$

$$F_z = 0 \quad (25)$$

$$\varsigma = 0 \quad (26)$$

$$T = T_0 \quad (27)$$

$$P = P_0, \quad (28)$$

and our exterior boundary conditions are

$$\kappa_R P = \frac{2}{3} \Omega^2 z \quad (29)$$

$$F_z = \sigma T^4 \quad (30)$$

$$\varsigma = \Sigma, \quad (31)$$

where  $\kappa_R$  is the Rosseland mean opacity.

### 3.5 Thermal equilibria: the S-curves

Before presenting outburst light curves based on the physical models discussed in the previous two sections we briefly discuss the properties of the disc's thermal equilibria. We consider two MRI-based models, DIMa and DIMRI, and compare them to the standard DIM. DIMa adopts the same vertical structure assumptions as the standard DIM, but uses the MRI-based  $\alpha(T_{\text{eff}})$  prescription of equations (5)-(6) discussed in section 2. DIMRI also uses this MRI-based  $\alpha$

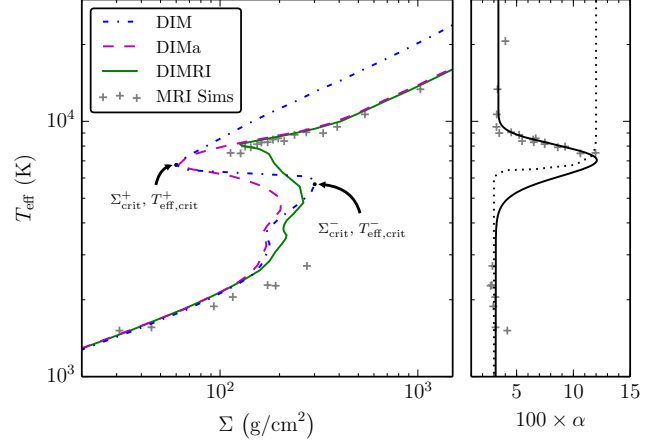


**Figure 8.** Left: Loci of thermal equilibria in the  $T_{\text{eff}}$  vs. surface mass density  $\Sigma$  plane (the “S-curve”) at radius  $R = 1.25 \times 10^{10}$  cm for the standard DIM (blue), DIMa (magenta) and DIMRI (green). The MRI simulation results are gray crosses (one point for each stable simulation). Additionally, the critical points  $(\Sigma_{\text{crit}}^+, T_{\text{eff,crit}}^+)$  and  $(\Sigma_{\text{crit}}^-, T_{\text{eff,crit}}^-)$  are marked for DIM. Right: The MRI-based  $\alpha(T_{\text{eff}})$  fit from Figure 1 plotted sideways in solid black (DIMa and DIMRI both use this fit) with the results from the same MRI simulations from the left plotted as gray crosses. Equation (1) for the standard DIM, with  $\alpha_c = 0.03$  and  $\alpha_h = 0.12$ , is plotted as the dotted black line.

prescription, combined with the MRI-based vertical structure equations (19)-(31) summarized in section 3.4. Figure 8 illustrates the differences in the S-curves produced by these models at radius  $R = 1.25 \times 10^{10}$  cm around a  $0.6M_\odot$  white dwarf.

The most important parameters emerging from the S-curves shown in Figure 8 are the critical surface mass densities  $(\Sigma_{\text{crit}}^+, \Sigma_{\text{crit}}^-)$  and effective temperatures  $(T_{\text{eff,crit}}^+, T_{\text{eff,crit}}^-)$  at the ends of the (upper, lower) branches, marking the points where (cooling, heating) transitions occur. In particular, the quotient of critical surface mass densities,  $Q\Sigma_{\text{crit}} \equiv \Sigma_{\text{crit}}^-/\Sigma_{\text{crit}}^+$ , plays an important role in determining the shape of the outburst lightcurve. It is therefore worth noting that  $Q\Sigma_{\text{crit}}$  is different for all of the S-curves, with DIM having the largest  $Q\Sigma_{\text{crit}}$ . Despite our efforts, there is still a basic discrepancy between the actual MRI simulation data and the DIMRI S-curve in Figure 8. Both branches of the simulation S-curve extend a little further in  $\Sigma$ , leading to a larger  $Q\Sigma_{\text{crit}}$  compared to that of DIMRI, and  $T_{\text{eff,crit}}^-$  is significantly larger in DIMRI on the lower branch. The mismatch on the upper branch can be explained by our choice of  $\alpha_{\text{ml}} = 6$ . As an annulus in outburst approaches the critical point  $(\Sigma_{\text{crit}}^+, T_{\text{eff,crit}}^+)$  the role of convection increases and presumably  $\alpha_{\text{ml}} = 6$  becomes increasingly less adequate. This is because the high value of  $\alpha_{\text{ml}}$  that we adopt is due to radiation dominated episodes in the intermittent convection, which become less prominent as the annulus reaches the end of the upper branch. One possible solution would be to decrease  $\alpha_{\text{ml}}$  towards the tip of the upper branch in the DIMRI, and this may be worth exploring in the future. We show how adopting a smaller constant value of  $\alpha_{\text{ml}}$  in DIMRI affects the outburst lightcurves below.

There are several issues which contribute to the mismatch between the simulation data and DIMRI on the lower



branch, and these all stem from the fact that we have been unable to find stable thermal equilibria in the simulations for effective temperatures higher than 3000 K. At such low temperatures, the opacities are so small that these equilibria are only marginally optically thick, with midplane optical depths  $\tau \lesssim 5$ . This may be a problem given that the simulations assume flux limited diffusion which may not accurately treat radiation transport at such low optical depths. The corresponding DIM models (i.e. DIM, DIMa, DIMRI) at these low temperatures also have low optical depths. As a consequence, the density at the photosphere (the exterior boundary condition) is a significant fraction of the central density implying that a large fraction of mass ( $\sim 10 - 50\%$ ) is ignored/neglected<sup>7</sup>. This missing mass likely has a significant impact on the temperature and density profiles of DIM models and is, at least partly, responsible for the miss-match between the DIMRI curve and the simulation data on the lower branch of the S-curve. The influence that this missing mass has on the temperature profiles may also explain why the DIMRI models near the end of the lower branch are convective (which is why the DIMRI S-curve turns up at  $\Sigma \approx 180 \text{ g cm}^{-2}$  in Figure 8), while there is no convection in any of the lower branch MRI simulations. Again, we have been unable to find any stable thermal equilibria at higher temperatures on the lower branch, where the opacities would be higher and missing mass would be less of an issue in the DIM models. However, there is perhaps an even bigger problem with the simulations on the lower branch, and that is that they neglect non-ideal MHD effects. As we demonstrate in Appendix A, Ohmic resistivity and the Hall term are likely to be important here, and so this also casts uncertainty on the lower branch results, and specifically the critical point of the lower branch ( $\Sigma_{\text{crit}}^-, T_{\text{crit}}^-$ ) which contributes to the determination of  $Q\Sigma_{\text{crit}}^-$ . Future work will have to account for these effects on the lower branch. Our focus here, however, is to see whether the variation in  $\alpha$  on the upper branch that has been found in the simulations can produce reasonable dwarf nova light curves.

Coming to the differences between our variants of the DIM, we first note that  $\Sigma_{\text{crit}}^-$  and  $T_{\text{eff,crit}}^-$  at the end of the lower branch are much higher on the classic DIM S-curve compared to both the DIMa and DIMRI S-curves, consequently DIM has the largest  $Q\Sigma_{\text{crit}}^-$ . As DIMa shares exactly the same vertical structure assumptions and equations as the classic DIM, this can only be due to the different alpha-prescriptions between the two models (equations 5-6 and equation 1, respectively). Recall from Figure 1 that our fit to the simulation data has  $\alpha$  starting to increase at  $T_{\text{eff}} \sim 4000 \text{ K}$ , roughly indicating the end of the lower branch. By contrast, the choice of  $T_{\text{crit}}^+$  in the classic DIM equation (1) corresponds to a much higher effective temperature ( $\sim 6000 \text{ K}$ ) at the end of the lower branch.

It should be noted that we have no simulation data for  $3000 \text{ K} \lesssim T_{\text{eff}} \lesssim 7000 \text{ K}$  in Figure 1, precisely because the simulations failed to produce stable thermal equilibria in this

range. Therefore, our fit in equations 5-6 has some flexibility in this temperature range. In principle, we could have fit the simulation data in Figure 1 with a function that keeps  $\alpha$  low until the effective temperature increases above 6000 K, and that would bring the lower branches of the DIMa and DIM S-curves into much better agreement. However, simulation ws0467 shown in Figure 4, was started near the end of the lower branch at  $T_{\text{eff}} \simeq 3000 \text{ K}$  and underwent runaway heating<sup>8</sup>. Hence our fits (equations 5-6) produce S-curves that better represent the behavior observed in the simulations.

Another alternative to achieve agreement on the lower branch is to reduce  $T_{\text{c0}}$  in the classic DIM. This has actually already been done by Hameury (2002), who modified this parameter to 8000 K, thereby producing a lower branch that only extended up to an effective temperature of 3000 K. This modification produces very similar outburst light curves, except that the quiescent light curves are flatter in shape, which actually may agree somewhat better with observations (Hameury 2002). Whether the low  $T_{\text{eff,crit}}^-$  can be claimed as a success of the MRI simulations will require a full treatment of the non-ideal MHD effects that have so far been neglected, but are likely to be crucial in the quiescent state, and hence will likely shift the end of the lower branch.

As we discuss in more detail below, the new simulation-based vertical structure equations (most importantly the different  $\alpha_{\text{mi}}$ ) are the reason DIMRI has a different location for the end of the upper branch than DIM and DIMa in Figure 8. In fact, if we plot a DIMRI S-curve with  $\alpha_{\text{mi}} = 1.5$ , the end of the upper branch matches that of the DIM and DIMa S-curves. The very large effective mixing length parameter  $\alpha_{\text{mi}} = 6$  used in DIMRI results in more efficient convective transport, which flattens the temperature profile thus increasing  $T_{\text{eff}}$  for a fixed midplane temperature  $T_{\text{c}}$ . Because the opacity is largely determined by  $T_{\text{c}}$ , it is  $T_{\text{c}}$  which determines where the end of the upper branch occurs. For radiative cooling the effective and central temperatures are related through

$$T_{\text{c}} = \left( \frac{3\tau_{\text{tot}}}{8} \right)^{1/4} T_{\text{eff}}, \quad (32)$$

where  $\tau_{\text{tot}}$  is the total (vertical) disc opacity (see e.g. Dubus et al. 1999; Kotko et al. 2012). For a fully ionized disc the Rosseland opacity is  $\kappa \sim \Sigma H^{-1} T_{\text{c}}^{-7/2} \text{ cm}^2/\text{g}$  from which follows the well known (Shakura & Sunyaev 1973) relation  $T_{\text{eff}} \propto \Sigma^{5/14}$ . Recombination breaks this relation and changes its slope while convection enhances cooling. The result is that the upper branch ends at higher effective temperature, and hence higher surface density.

## 4 OUTBURST LIGHT CURVES

### 4.1 The outburst cycle

During the low luminosity “quiescent” phase of a dwarf nova cycle, the effective temperature in the whole disc is lower

<sup>7</sup> These inaccuracies do not affect standard DIM models of real outbursts, because in these models the disc never cools down to temperatures at which these discrepancies appear. In the standard DIM one simply tunes  $\alpha_{\text{h}}$  and  $\alpha_{\text{c}}$  to obtain the required ratio of the critical surface densities.

<sup>8</sup> Although this helps constrain the end of the lower branch, it is numerically challenging to further resolve the critical point ( $\Sigma_{\text{crit}}^-, T_{\text{crit}}^-$ ), as the simple act of relaxing from the initial conditions could push a simulation too far from ( $\Sigma_{\text{crit}}^-, T_{\text{crit}}^-$ ) to obtain a thermal equilibrium.

than  $T_{\text{eff,crit}}^-$  (the disc is cold). The mass accretion rate is not constant across the cold disc so the disc accumulates matter, increasing its temperature and surface density (each disc annulus moves up the lower branch of its local S-curve). Finally, at some radius,  $R_0$ , the accumulation time becomes shorter than the viscous time, and the ionization of gas becomes so significant that the local cooling mechanisms become inefficient and thermal equilibrium is lost. The annulus at  $R_0$  undergoes rapid heating and makes the transition to the hot state (upper branch of its local S-curve). A narrow fully-ionized region of high viscosity has just formed at  $R_0$ , and is surrounded by cold matter. This induces a steep radial temperature gradient and the formation of the heating front, indicating the beginning of an outburst. Additionally, a spike in the  $\Sigma$  profile arises as a consequence of different viscous efficiencies in the hot and cold parts of the disc: the low viscosity outside the hot annulus provides insufficient outwards angular momentum transport to prevent further accumulation of mass at  $R_0$ . These steep  $\Sigma$  and  $T_{\text{eff}}$  gradients in the heating front cause matter and heat to diffuse to the adjacent annuli, forcing their transition to the hot state. The hot region in the disc widens as the heating front propagates through the disc causing the luminosity to rise. The elevated mass accretion rate in the hot region reduces the surface density behind the heating front and enhances the mass inflow to the inner disc region<sup>9</sup>.

Once the heating front reaches the outer disc edge, the disc is fully ionized and reaches its maximum brightness (the outburst maximum). In the DIM, the minimum critical surface density  $\Sigma_{\text{crit}}^+$  at the end of the upper branch of the local S-curve is approximately proportional to radius  $R$  (Hameury et al. 1998), causing  $\Sigma_{\text{crit}}^+$  to be highest at  $R_{\text{out}}$ . Consequently  $\Sigma$  manages to only rise slightly above this critical value near  $R_{\text{out}}$  as the heating front passes and it falls below the critical value almost immediately after the front dissipates. At the radius where this happens the cooling is strongly enhanced by the change of opacities when  $T_{\text{eff}} < T_{\text{eff,crit}}^+$  and  $\Sigma$  and  $T_{\text{eff}}$  gradients lead to the formation of the cooling front. The inward propagation of the cooling front through the disc leads to the observed outburst decay.

The cooling front develops at the outer disc edge almost at the same time as the heating front disappears, allowing no time for the mass accumulated in the outer parts of the disc to arrive at the inner disc radius before the cooling front sets in, even though the mass accretion rate everywhere in the hot disc has increased beyond the mass transfer rate from the secondary. The surface density profile at the outburst maximum is not yet proportional to  $R^{-3/4}$  as expected in a hot stable disc. Therefore, even after the development of the cooling front, the mass accretion rate near the inner disc edge still increases until the mass excess from the outer disc region has traveled through the whole disc and has been accreted onto the white dwarf (see Figure 13 and for more details Kotko & Lasota 2012). Only after this will the hot region ahead of the cooling front reach the hot stable state

where the constant mass accretion rate is of order  $\dot{M}_{\text{tr}}$ , the mass transfer rate from the secondary.

## 4.2 Reflares

Due to the high  $\dot{M}_{\text{tr}}$  and low  $\alpha_c$ , the disc may accumulate a lot of mass during the quiescent phase and rise to an outburst. If the viscosity in the hot disc is not efficient enough (i.e. when  $\alpha_h$  is relatively low) to redistribute the mass excess accumulated during the previous outburst phases to the inner region (where it can be accreted), or if the critical points  $(\Sigma_{\text{crit}}^-, T_{\text{crit}}^-)$  and  $(\Sigma_{\text{crit}}^+, T_{\text{crit}}^+)$  are too close (i.e.  $Q\Sigma_{\text{crit}}$  is too small), the fronts propagating in the disc (both cooling and heating) may be stopped before arriving at either of the two disc edges. This gives rise to the appearance of reflares in the outburst lightcurves. As we discuss below, all our MRI-based models exhibit this phenomenon, and we therefore begin with a brief description of the cause: it is the confluence of the small  $\alpha_h$  high on the upper branch as well as the small  $Q\Sigma_{\text{crit}}$  that is responsible for these reflares.

As a cooling front propagates inward, the high viscosity of the hot matter inside the cooling front contrasted with the low viscosity outside the cooling front causes an outward diffusion of matter across the front. This in turn causes a deficit in surface density within the front itself, followed by an enhanced surface density in the cold region behind (outside) the front. Hence, as the cooling front moves inward in radius, at some point the post-front  $\Sigma$  may become high enough to cross the critical value  $\Sigma_{\text{crit}}^-$  at the end of the lower branch of the local S-curve. It is here where it is clearest that the low  $\alpha_h$  and the lack of sufficient separation between  $\Sigma_{\text{crit}}^-$  and  $\Sigma_{\text{crit}}^+$  (i.e. too small  $Q\Sigma_{\text{crit}}$ ) conspire against the smooth propagation of a cooling front by creating a mass excess outside the front and setting a low critical threshold respectively.

In this situation a new heating front arises and starts to move outwards. The matter heated by this newly formed front flows at a high rate into the zone of the cooling front, increasing its temperature and surface density. This inflow of hot gas eventually destroys the cooling front and only a heating front is left. As a result, the inward propagating cooling front behaves as if it is reflected into an outward propagating heating front before it arrives at the inner edge. A similar mechanism can cause reflection of the heating front propagating toward the outer disc radius. If the post-front  $\Sigma$  remains close to  $\Sigma_{\text{crit}}^+$  the elevated accretion rate in the hot region behind the front may cause  $\Sigma$  to fall below the critical value and a cooling front will start to form. The reduced transport of the angular momentum through the emerging cold zone finally stops the propagation of the heating front and a newly formed cooling front will move inward. These reflections produce a reflare pattern in the outburst lightcurves (see sawtooth-like features in Figure 9), which are not observed in standard dwarf novae. As reviewed in section 4.3 of Lasota (2001), reflares are a common feature of the DIM, and one must work to get rid of them by choosing appropriate values of  $\alpha_h$  and  $\alpha_c$  in order to agree with the smooth observed light curves. As we will see shortly, reflares are also a generic feature of all our MRI-based lightcurves. However, it is important to reemphasize that the reflares (and the details of outbursts) are dependent on where the lower branch ends; a detail we do not claim to model accurately.

<sup>9</sup> We describe here an *inside-out* outburst. For high mass-transfer rates, outbursts can be of *outside-in* type, i.e. the heating front propagates inwards from the disc outer regions (see e.g. Lasota 2001).

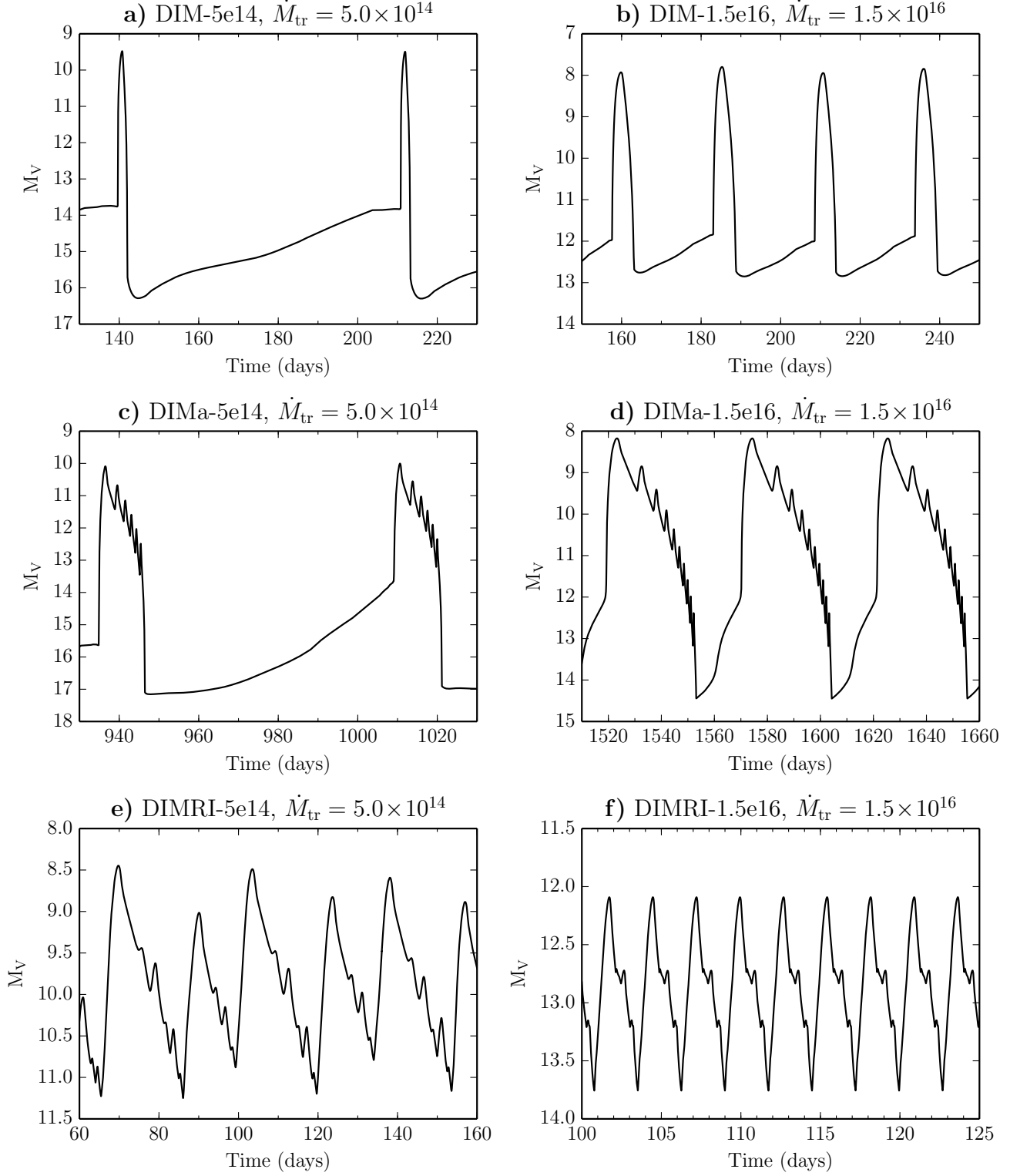


**Figure 9.** Visual magnitude lightcurves for six of the models listed in Table 1. The sawtooth-like features are reflares. The units for the listed mass transfer rates are g/s.

Model	$\dot{M}_{\text{tr}}$ [g/s]	$A_{\text{outb}}$	$T_{\text{outb}}$	$T_{\text{quiesc}}$	Figure
DIM-5e14	$5 \times 10^{14}$	5.4	2.3	47.3	9a
DIM-1.5e16	$1.5 \times 10^{16}$	4.6	6.3	11.6	9b
DIMa-5e14	$5 \times 10^{14}$	7	11.6	46.4	9c
DIMa-1.5e16	$1.5 \times 10^{16}$	6.3	50	0	9d
DIMRI-5e14	$5 \times 10^{14}$	1.7	2.8	0	9e
DIMRI-1.5e16	$1.5 \times 10^{16}$	2.6	19.9	0	9f
DIMRI- $\alpha_{ML} = 1.5$	$5 \times 10^{14}$	7.7	17.3	60.1	10
DIMRI-6e13	$6 \times 10^{13}$	3.2	1.9	7	11
DIMRItr-1.5e16	$1.5 \times 10^{16}$	3.4	14.6	4.7	12

**Table 1.** The parameters of the outbursts measured in our calculated lightcurves.  $A_{\text{outb}}$  is the outburst amplitude in magnitudes,  $T_{\text{outb}}$  is the outburst duration time in days and  $T_{\text{quiesc}}$  is the quiescence time in days, i.e. the time elapsed between the end of an outburst and the beginning of the next. The last column lists the figure where the lightcurve for a given model can be found.

### 4.3 Results

The outburst properties depend on disc viscosity and the parameters characterizing a binary. For the new DIMRI to be considered as a possible replacement for the standard DIM, it should reproduce the basic features of dwarf novae lightcurves such as outburst amplitude, outburst duration and quiescence duration.

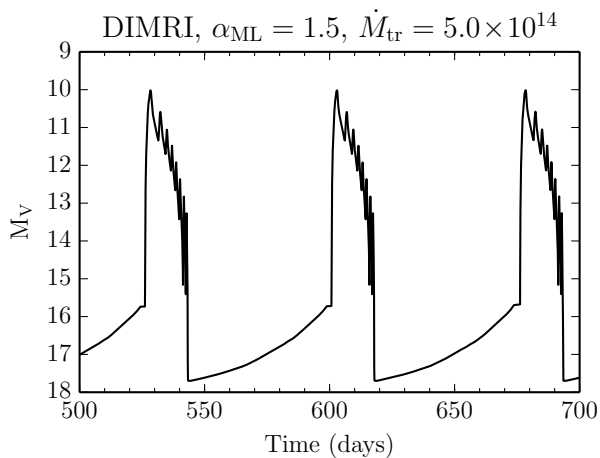
To better understand how the new  $\alpha$ -prescription and the new disc vertical structures introduced into the classical DIM influence outburst light curves, we calculated these light curves using three models: DIMRI, DIM with  $\alpha$  as a function of  $T_{\text{eff}}$  (DIMa) and classic DIM with  $\alpha_c = 0.03$  and  $\alpha_h = 0.12$ . All models were calculated for the same set of parameters: a primary mass  $M_1 = 0.6 M_{\odot}$ , the disc inner radius  $R_{\text{in}} = 8.67 \times 10^8$  cm, and the circularization radius  $R_{\text{circ}} = 2.85 \times 10^{10}$  cm. In addition we run the calculation for two different values of the mass transfer rate:  $\dot{M}_{\text{tr}} = 1.5 \times 10^{16}$  g/s and  $\dot{M}_{\text{tr}} = 5 \times 10^{14}$  g/s for each model (see Table 1). In all models the outer disc radius is variable due to the fact that we take into account the tidal force acting between the secondary star and the disc. For the models in this paper, the average outer disc radius is  $\langle R_{\text{out}} \rangle = 4.6 \times 10^{10}$  cm.

Analyzing the differences between the lightcurves (see Figures 9-12) gives insight into the physical implications of our modifications to the DIM. One subtle difference between the classic DIM lightcurves and the MRI based lightcurves is that the MRI based ones are not strictly periodic. We do not understand why the new  $\alpha$  prescription causes this. One possibility is that the disc needs much more time to relax with this prescription. Conversely, the most striking difference between the DIM and the two other model light curves is that the outburst decay in DIM is smooth while in DIMRI and DIMa the outburst decay has small amplitude brightness variations characteristic of reflares (compare Figure 9c-f with Figure 9a,b). The reason that reflares do not appear in the DIM but are present in the two other models is connected to our  $\alpha$ -prescription, but is also tied to our uncertainties on the lower branch, specifically the location of the critical point ( $\Sigma_{\text{crit}}^-, T_{\text{crit}}^-$ ). In the DIM,  $Q\Sigma_{\text{crit}}$  is

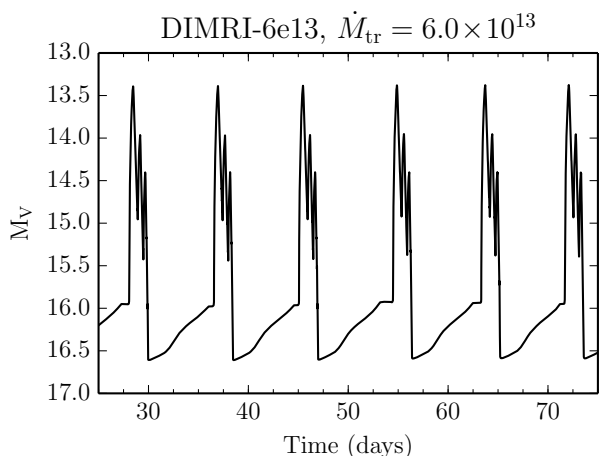
larger than the other models and  $\alpha$  maintains its high value ( $\alpha_h = 0.12 \gg \alpha_c$ ) in the whole hot part of the disc until the cooling front passage. In the models where  $\alpha$  is a function of effective temperature, the higher viscosity is present in a much more narrow region, i.e. in which the central temperature is higher than  $T_{\text{crit}}^-$  but lower than  $5 \times 10^4$  K. Therefore, the mass in the inner disc region is accreted at a lower rate than in the DIM due to the lowered viscosity in the high temperature regime, leading to an excess of mass behind (outside) cooling fronts. It is the combination this effect coupled with the small  $Q\Sigma_{\text{crit}}$  which is directly responsible for the reflares seen in DIMa and DIMRI. Furthermore,  $Q\Sigma_{\text{crit}}$  as determined by MRI simulations is actually larger than that found in DIMRI, which suggests that DIMRI is more susceptible to reflares than what the simulation data imply.

Figure 13 shows how the higher surface mass density in the inner disc and smaller  $Q\Sigma_{\text{crit}}$  in DIMa leads to reflections of the inward propagating cooling front and reflares. The first epoch shown (the red curves labeled 1) corresponds to the time when the outward propagating heating front has just arrived in the outer disc, which is why there is a spike in surface density and bump in midplane temperature at  $R \sim 1.3 \times 10^{10}$  cm. By this time an inward propagating cooling front has already been launched, and is located at  $\simeq 7.6 \times 10^9$  cm where the surface density has reached the critical surface density  $\Sigma_{\text{crit}}^+$  on the upper branch of the local S-curve. As the front propagates inward from 1 (red) to 2 (green) to 3 (blue), the gradients in viscosity cause outward mass diffusion, thereby producing a rarefaction in surface density down to  $\Sigma_{\text{crit}}^+$  within the cooling front, followed by an enhanced surface density behind (outside) the front. Because the inner disc in the outburst state has such a high surface density due to the *low* values of  $\alpha$  high up on the upper branch relative to the DIM, the post-front excess in surface mass density is also high, and eventually, at epoch 4 (magenta) at  $R = 4.6 \times 10^9$  cm, reaches the critical surface density  $\Sigma_{\text{crit}}^-$  at the end of the lower branch of the local S-curve (highlighting the role of small  $Q\Sigma_{\text{crit}}$ ). This triggers a heating front which then propagates outward, as evident in epoch 5 (black) at  $R = 5.3 \times 10^9$  cm.

Hence, directly as a consequence of the small  $\Sigma_{\text{crit}}^-$  (or



**Figure 10.** Light curves calculated from DIMRI but for  $\alpha_{ml} = 1.5$ ;  $\dot{M}_{tr} = 5.0 \times 10^{14} \text{ g s}^{-1}$ . Compare with Fig. 9e.



**Figure 11.** Light curves calculated from DIMRI with  $\dot{M}_{tr} = 6.0 \times 10^{13} \text{ g s}^{-1}$ .

alternatively small  $Q\Sigma_{crit}$ ) combined with the low  $\alpha$ 's and resulting higher surface densities in the inner disc in outburst, the cooling front that would normally cause a transition back to quiescence propagates instead with difficulty, through a sequence of reflections seen as reflare in the light curve. In contrast, in the DIM with suitably chosen  $\alpha_h$  and  $\alpha_c$ , there is a larger  $\Sigma_{crit}^-$  making it harder to trigger a reflare. Additionally, the mass diffusion and accretion during the outburst is much higher and the inner disc is able to process sufficient mass to lower the inner surface density and avoid the appearance of the reflare during the outburst decay. The contested propagation of the cooling front in DIMa causes the outburst decay phase to last longer compared to DIM (for example compare Figure 9a with Figure 9c). During this time more mass is being accreted onto the white dwarf in the DIMa, leaving the disc less massive and less luminous than in the DIM at the end of outburst. This results in a higher amplitude outburst for the DIMa, which highlights the effect reflare have on outbursts.

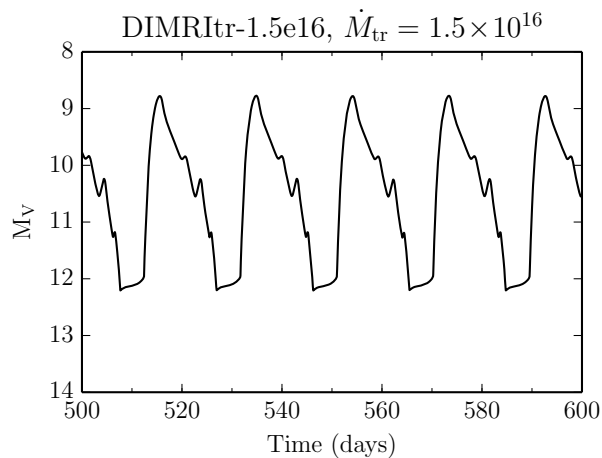


**Figure 12.** Light curves calculated from DIMRI with inner disc radius truncated by the magnetic field with magnetic moment  $\mu = 8 \times 10^{30} \text{ G cm}^3$  for  $\alpha_{ml} = 6.0$ ;  $\dot{M}_{tr} = 1.5 \times 10^{16} \text{ g s}^{-1}$ . As can be seen by comparing this to Fig. 9f, the truncation of the inner disc results in the appearance of quiescence and more regular outbursts.

The difference in light curves between DIMRI and DIMa is due to the different  $\alpha_{ml}$  values and different dissipation profiles. The mixing length parameter  $\alpha_{ml}$  is the most important difference, as can be seen by comparing Figure 9e with Figure 10, which presents the same DIMRI calculation but with  $\alpha_{ml}$  restored to its traditional value of 1.5. Convection sets in close to the point where the cold branch of the S-curve ends which leaves this point sensitive to  $\alpha_{ml}$ . This effect is even stronger on the critical point where the hot branch starts, as this is where convection is the strongest. Higher values of  $\alpha_{ml}$  shift both critical points at which the S-curve bends closer together, leading to a smaller  $Q\Sigma_{crit}$ . This alters the global behavior of the disc and the outburst properties: the decay from the outburst in a disc with  $\alpha_{ml} = 6$  starts at higher  $\Sigma$  and higher  $T_{eff}$ , and less mass is accreted and accumulated in the disc during the outburst cycle. Therefore, more efficient convection produces outbursts that are more frequent and of lower amplitude, and even lack quiescent phases. While it is important to note that this lack of quiescence may be related to uncertainties in the end of the lower branch, there are other ways out. In the discussion below, we examine a few options to restore or modify quiescence.

The comparison of DIMRI with  $\alpha_{ml} = 1.5$  and DIMa (Figure 10 and Figure 9c) highlights the importance of changing the dissipation profile, as this is the only difference between these two models. The main difference is that the outbursts in DIMRI with  $\alpha_{ml} = 1.5$  are wider and the quiescence is longer than in the DIMa light curve.

Changing the mixing length parameter is not the only way to increase the outburst amplitude and restore quiescent phases to the DIMRI models. Increasing the mass transfer rate, while all other parameters are fixed, makes the disc hotter and denser. This means that the surface density everywhere in the quiescent disc is closer to the critical value and the disc luminosity is higher. The result is more frequent lower amplitude outbursts for higher mass transfer rate regardless of model, as illustrated by comparing the two mass

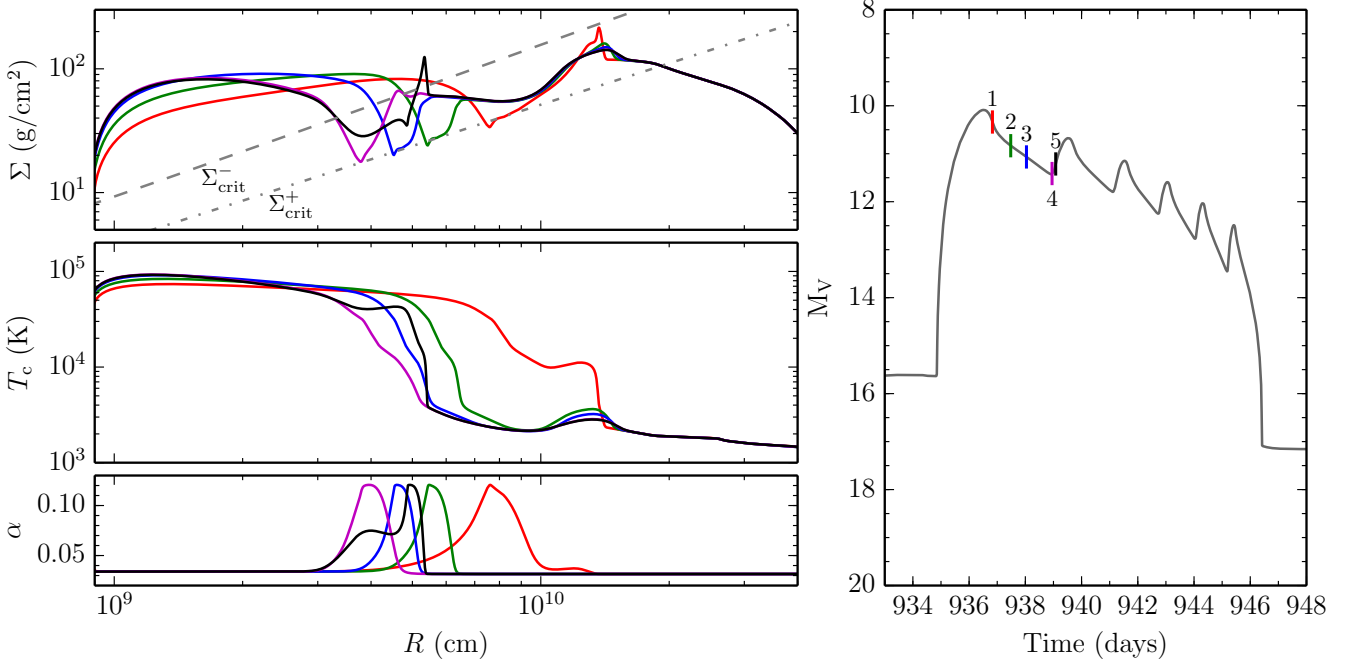


**Figure 13.** Left panels: Radial profiles of surface density (top), midplane temperature (middle), and  $\alpha$ -parameter (bottom) during the initial decay from outburst for the DIMa calculation with  $\dot{M} = 5 \times 10^{14} \text{ g s}^{-1}$ . Right panel: Zoom of the first outburst in the lightcurve Figure 9(c). Different successive times 1-5 are shown by different colors as indicated, with 1 (red) being the first and 5 (black) being the last. It is important to note that  $\alpha$  is small for  $R < 3 \times 10^9 \text{ cm}$  for all epochs shown despite the fact that the disc is in outburst, because we are high on the upper branch here. This results in the elevated surface mass density that can be seen in the inner disc. As the cooling front (the dip/rarefaction in  $\Sigma$  located at  $R \approx 7.6 \times 10^9 \text{ cm}$  in epoch 1) propagates inwards through the disc, mass is redistributed from ahead of the front where  $\Sigma$  is high to the post-front region. Eventually, the post-rarefaction surface density crosses the critical surface density  $\Sigma_{\text{crit}}^-$  at the end of the lower branch of the local S-curve. This occurs approximately at epoch 4 (magenta), which is when the inward propagating cooling front is reflected into the heating front seen at  $R \approx 5.3 \times 10^9 \text{ cm}$  in epoch 5 (black). This figure clearly shows that either further separating  $\Sigma_{\text{crit}}^-$  and  $\Sigma_{\text{crit}}^+$  (i.e. increasing  $Q\Sigma_{\text{crit}}$ ) or reducing the excess mass in the inner disc by increasing  $\alpha$  high on the upper branch could help alleviate reflares.

transfer rates shown in Figure 9 for each of our three models. Hence merely reducing the mass transfer rate in the DIMRI model can increase the outburst amplitude and restore quiescent phases. If one sets  $\dot{M}_{\text{tr}}$  as low as  $\dot{M}_{\text{tr}} = 6 \times 10^{13} \text{ g/s}$  in the DIMRI (with  $\alpha_{\text{ml}} = 6$ ) the elapsed time between two consecutive outbursts starts to be longer and also the outburst amplitude rises (see Table 1 and Figure 11). Note that for such a low  $\dot{M}_{\text{tr}}$ , the discs in DIM and DIMa become cold and stable.

There is yet another alternative way to restore quiescence in the DIMRI light curves. Observed X-ray fluxes in quiescent dwarf novae are far too large compared to what models predict. A solution to this problem is a truncation of the inner disc. Numerical calculations by Hameury et al. (2000) and Schreiber et al. (2003) confirm that truncating the inner disc has substantial influence on the dwarf nova lightcurves and may solve the discrepancy between observations and theory. This truncation may be caused by the magnetic field of the primary white dwarf. A white dwarf magnetic field in the range  $10^4 - 10^7 \text{ G}$  (which translates to a magnetic moment  $\mu \approx 1 - 10^3 \times 10^{30} \text{ G cm}^3$ ) is sufficient for the magnetic pressure close to the white dwarf to exceed the gas and ram pressures of the infalling matter during the quiescent phase of the dwarf nova cycle. The inner disc radius is therefore pushed away from the white dwarf to a

radius  $R_M$  (e.g. Frank et al. 2002):

$$R_{\text{in}} = R_M = 9.8 \times 10^8 \dot{M}_{\text{tr}15}^{-2/7} M_1^{-1/7} \mu_{30}^{4/7} \text{ cm} \quad (33)$$

where  $\mu_{30}$  is the magnetic moment in units of  $10^{30} \text{ G cm}^3$ ,  $M_1$  is the mass of the primary in solar masses and  $\dot{M}_{15}$  is the mass accretion rate in units of  $10^{15} \text{ g/s}$ . During outburst the situation changes, as the higher mass accretion rate sharply increases the ram pressure of matter which then dominates the magnetic pressure, and the inner edge of the disc approaches the surface of the white dwarf. Taking into account the variation in inner disc radius according to Eq.(33) restores the quiescent phase in the simulated DIMRI light curves (compare Figures 9f and 12).

## 5 DISCUSSION

There are four main aspects of observed dwarf nova light curves which need to be reproduced in order to have a successful theoretical model: quiescence duration, outburst amplitude, outburst duration, and shape. For the most part our MRI based models DIMa (which differ from the DIM models only by incorporating the MRI simulation based  $\alpha(T_{\text{eff}})$ ) and DIMRI can reproduce these attributes, with the notable exception of reflares. These reflares are the result of two contributing factors. Namely, the small ratio of the surface densities at the ends of the lower and upper branches,  $Q\Sigma_{\text{crit}}$ ,



and the low value of  $\alpha$  found high up on the upper branch. This low  $\alpha$  causes an excess of surface mass density  $\Sigma$  in the inner disc. Consequently, as a cooling front propagates inward through the disc it accumulates substantial mass in the post-front region, and due to the small  $Q\Sigma_{\text{crit}}$ , this post-front excess in  $\Sigma$  easily surpasses the critical value,  $\Sigma_{\text{crit}}^-$ , and initiates a reflare. The reflare created by this series of events tend to prolong the decay from outburst. We have found two mechanisms which help to hasten this elongated decay from outburst: reducing the mass transfer rate and truncation of the inner disc by a white dwarf magnetic field (Figures 11-12). However, these tweaks are merely attempts to treat the symptoms caused by the greater underlying issues mentioned above<sup>10</sup>.

It is important to remember that  $Q\Sigma_{\text{crit}}$  is determined by the physics of both the upper and lower branches, and the lower branch physics is very uncertain. The simulations were produced with the ideal MHD and flux limited diffusion approximations. While these are reasonable on the upper branch, the lower branch is a different story. Optical depths along the lower branch are low ( $\tau \lesssim 5$ ) bringing into question our usage of the flux limited diffusion approximation. Moreover, non-ideal effects, particularly resistivity and Hall effects (Bai 2014; Lesur et al. 2014, Appendix A) are important on the lower branch where the ionization fraction is low. This strongly motivates the need to pursue non-ideal MHD simulations of the lower branch, and as in protostellar discs (Igea & Glassgold 1999), it may be necessary to account for irradiation by ionizing x-rays from the boundary layer between the white dwarf and the accretion disc, because any source of ionization has the potential to significantly modify non-ideal MHD effects. MRI turbulence may only exist in the irradiated surface layers, possibly leaving a magnetically driven laminar flow in the resistive “dead zone” interior (Turner & Sano 2008). Small amounts of hydrodynamic angular momentum transport associated with thermal convection (Lesur & Ogilvie 2010) may also exist. However, it may turn out that none of these local mechanisms is sufficient to explain the quiescent state, and that something involving more global physics is required. For example, recent isothermal and adiabatic global simulations by Ju et al. (2016) suggest that spiral waves excited by the tidal field of the donor star may contribute significantly to the angular momentum transport in the quiescent state, and this physics cannot be captured by a local stress-pressure relation. All this speculation, again highlights the uncertainty in  $Q\Sigma_{\text{crit}}$ , and the need for the inclusion of non-ideal effects on the lower branch.

Even with this uncertainty, however, we have found that enhancement of  $\alpha$  only near the end of the upper branch, where thermal convection happens, is capable of producing outbursts. This outcome is non-trivial and suggests that convection plays a major role in the outbursts of dwarf novae, and while important, convection may not be the end of the story. The low values of  $\alpha$  high up on the upper branch as found by Hirose et al. (2014), are a contributing factor in the appearance of reflare. As mentioned early on in this paper, MRI simulations with net vertical magnetic flux have

larger  $\alpha$  values (Hawley et al. 1995; Sano et al. 2004; Pessah et al. 2007). While we have considered a way of increasing  $\alpha$  with zero net vertical magnetic flux by the effects of hydrodynamic convection on MRI turbulence, there is no reason to view these explanations as mutually exclusive. Accordingly, simulations examining how net vertical magnetic flux modifies convection and the associated enhancement of  $\alpha$  found in Hirose et al. (2014) would be useful and may help alleviate reflare.

It is also important to note that we have not successfully incorporated all aspects of the physics observed in the simulations in our attempts to model outburst light curves here. The MRI-based physics that we have succeeded in incorporating into the DIM has not produced S-curves that completely agree with the simulation data (cf. Figure 8). Both the upper and lower branches of the MRI simulation S-curve are extended slightly further in  $\Sigma$  compared to DIMRI. This implies that DIMRI should have a larger  $Q\Sigma_{\text{crit}}$  which in turn would increase the amplitude and the quiescence duration and may reduce or even alleviate the reflare.

Moreover, it is clear that the MRI simulations exhibit some time dependent behavior (e.g. intermittent convection) that the DIM simply is incapable of handling. During the convective epochs the Shakura & Sunyaev (1973)  $\alpha$  parameter is enhanced and also  $\alpha_{\text{ml}} \sim 1.5$ . To re-emphasize this,  $\alpha$  is significantly higher and  $\alpha_{\text{ml}}$  significantly lower during the intermittent convective epochs than their respective time averaged quantities. This has a significant impact on the evolution of an annulus as it transitions from quiescence to outburst<sup>11</sup>. Thermally unstable MRI simulations that are heating towards the hot branch are fully convective, with no intermittency. Therefore, when an annulus first makes it to the hot branch it will be fully convective and “see” an instantaneous S-curve which is characterized by the  $\alpha$  and  $\alpha_{\text{ml}}$  seen during convective epochs. This annulus will then evolve and after a few thermal times become better characterized by the time averaged values for  $\alpha$  and  $\alpha_{\text{ml}}$  and the associated “long-term” S-curve. Global MRI simulations of the propagation of heating and cooling fronts would obviously be of great interest, but are not yet viable for the dwarf nova problem.

We finally note that the quiescent state is also a problem for the DIM models (i.e. DIM, DIMa, DIMRI) presented here and historically in the standard DIM; see e.g. Lasota (2001). Our lower branch DIM models with  $T_{\text{eff}} < 3000$  K have low optical depths<sup>12</sup> ( $\tau \lesssim 5$ ) which leads to inaccuracies, most notably  $\sim 10 - 50\%$  of mass lying outside of the vertical boundary condition. However, until non-ideal effects are included in the lower branch simulations, it is futile to try and bring the simulation data and DIM models into better agreement here. This impacts the details of outburst lightcurves, most notably the occurrence of reflare. While these reflare are not observed in the outbursts of standard dwarf novae, we nevertheless recover outburst time

<sup>11</sup> We note that our shearing box simulations are local not only in the radial direction, but also in the azimuthal direction. Therefore, the time dependent behavior may be less manifest in observations where azimuthal variations are averaged.

<sup>12</sup> This does not occur in the classical DIM, because without the MRI-based constraints we have imposed in this paper  $\alpha_c$  and  $\alpha_h$  can be tuned to avoid this problem.

<sup>10</sup> Notice, however, that disc truncations is independently required by dwarf nova observations (see e.g., Lasota 2001).

scales and amplitudes comparable to those observed, implying that the simulation-based models of the upper branch are in good agreement with observations.

## 6 CONCLUSIONS

We have incorporated the convection-induced enhancement of  $\alpha$  close to the hydrogen ionization temperature that was discovered in MRI simulations by Hirose et al. (2014) into the DIM. This, for the first time, places the early inference by Mineshige & Osaki (1983); Smak (1984); Meyer & Meyer-Hofmeister (1984) that  $\alpha$  had to be larger in outburst in dwarf novae on a strong and clear theoretical foundation based on MRI turbulence. We have also shown how to incorporate aspects of the time-averaged vertical structure (dissipation profiles, intermittent convective heat transport) into the DIM. With suitable parameter choices and/or truncation of the inner disc by a white dwarf magnetic field, the resulting lightcurves are able to produce outburst and quiescent durations, as well as outburst amplitudes, that are consistent with observations of dwarf novae. Further work to actually fit particular dwarf nova systems with this model might be worthwhile.

A generic feature of our MRI-based  $\alpha$ -prescription is the appearance of reflares. These reflares are caused by the confluence of low  $\alpha$ 's high up on the upper branch and the small ratio of critical surface mass densities  $Q\Sigma_{\text{crit}}$ . Our biggest uncertainty in this work is the physics of the lower branch and consequently  $Q\Sigma_{\text{crit}}$ . This uncertainty primarily stems from the exclusion of important non-ideal MHD effects associated with the largely electrically neutral plasma on the lower branch. This gives us a clear motivation and direction for future work to address these inaccuracies in new simulations and to obtain a more realistic understanding of the lower branch and its end.

Additionally, while we have tried to incorporate MRI-based physics into the DIM, this has only been done for annuli in thermal equilibrium. We still do not understand how MRI physics might affect the propagation of heating and cooling fronts, and it is these that are responsible for reflares. MRI simulations in a more global geometry that can track the propagation of such fronts would of course be very illuminating, though such simulations appear to be challenging with current resources.

Finally, it is important to remember that reflares are also a common problem even in the standard DIM, where one is free to choose values of  $\alpha_h$  and  $\alpha_c$  to try and get rid of them (e.g. Lasota 2001). This freedom is of course an illusion, as the stresses are actually determined by the underlying physics of turbulence in the disc. The fact that applications of our MRI simulation results to the DIM give rise to reflares helps sharpen this problem by relating it more to the fundamental physics responsible for stresses in the disc.

## ACKNOWLEDGMENTS

We thank the anonymous referee for a constructive report that led to significant improvements in this paper. We also wish to acknowledge the seminal role of Jean-Marie

Hameury and Guillaume Dubus in developing the numerical methods necessary to accurately model lightcurves within the DIM.

Additionally, we also thank Jean-Marie Hameury for constructive feedback on this work. This research was supported by the United States NSF grant AST-1412417, the Polish NCN grants UMO-2013/08/A/ST9/00795 and UMO-2015/19/B/ST9/01099, and by Japan JSPS KAKENHI Grants 24540244 and 26400224, joint research project of ILE, Osaka University. JPL was supported in part by a grant from the French Space Agency CNES. OB thanks the International Space Science Institute in Bern for its support while this paper was being completed. Numerical calculations were partly carried out on the Center for Scientific Computing from the CNSI, MRL: an NSF MRSEC (DMR-1121053) and NSF CNS-0960316, and the Cray XC30 at CfCA, National Astronomical Observatory of Japan.

## REFERENCES

- Bai X.-N., 2014, *ApJ*, 791, 137
- Bai X.-N., Stone J. M., 2013, *ApJ*, 767, 30
- Balbus S. A., Hawley J. F., 1991, *ApJ*, 376, 214
- Balbus S. A., Hawley J. F., 1998, *Reviews of Modern Physics*, 70, 1
- Balbus S. A., Terquem C., 2001, *ApJ*, 552, 235
- Blaes O., Krolik J. H., Hirose S., Shabaltas N., 2011, *ApJ*, 733, 110
- Blaes O. M., Balbus S. A., 1994, *ApJ*, 421, 163
- Davis S. W., Stone J. M., Pessah M. E., 2010, *ApJ*, 713, 52
- Draine B. T., 2011, *Physics of the Interstellar and Inter-galactic Medium*
- Draine B. T., Roberge W. G., Dalgarno A., 1983, *ApJ*, 264, 485
- Dubus G., Hameury J.-M., Lasota J.-P., 2001, *A&A*, 373, 251
- Dubus G., Lasota J.-P., Hameury J.-M., Charles P., 1999, *MNRAS*, 303, 139
- Frank J., King A., Raine D. J., 2002, *Accretion Power in Astrophysics: Third Edition*
- Fromang S., Latter H., Lesur G., Ogilvie G. I., 2013, *A&A*, 552, A71
- Fromang S., Papaloizou J., Lesur G., Heinemann T., 2007, *A&A*, 476, 1123
- Guan X., Gammie C. F., 2011, *ApJ*, 728, 130
- Hameury J., Lasota J., Warner B., 2000, *A&A*, 353, 244
- Hameury J.-M., 2002, in Gänsicke B. T., Beuermann K., Reinsch K., eds, *The Physics of Cataclysmic Variables and Related Objects Vol. 261 of Astronomical Society of the Pacific Conference Series, The disc instability model.* p. 377
- Hameury J.-M., Menou K., Dubus G., Lasota J.-P., Hure J.-M., 1998, *MNRAS*, 298, 1048
- Hawley J. F., Balbus S. A., 1991, *ApJ*, 376, 223
- Hawley J. F., Gammie C. F., Balbus S. A., 1995, *ApJ*, 440, 742
- Hawley J. F., Gammie C. F., Balbus S. A., 1996, *ApJ*, 464, 690
- Hawley J. F., Guan X., Krolik J. H., 2011, *ApJ*, 738, 84
- Hirose S., 2015, *MNRAS*, 448, 3105

- Hirose S., Blaes O., Krolik J. H., Coleman M. S. B., Sano T., 2014, *ApJ*, 787, 1
- Hirose S., Krolik J. H., Stone J. M., 2006, *ApJ*, 640, 901
- Igea J., Glassgold A. E., 1999, *ApJ*, 518, 848
- Ju W., Stone J. M., Zhu Z., 2016, *ApJ*, 823, 81
- King A. R., Pringle J. E., Livio M., 2007, *MNRAS*, 376, 1740
- King A. R., Ritter H., 1998, *MNRAS*, 293, L42
- Kotko I., Lasota J.-P., 2012, *A&A*, 545, A115
- Kotko I., Lasota J.-P., Dubus G., Hameury J.-M., 2012, *A&A*, 544, A13
- Lasota J.-P., 2001, *NewAR*, 45, 449
- Lasota J.-P., Dubus G., Kruk K., 2008, *A&A*, 486, 523
- Lesur G., Ferreira J., Ogilvie G. I., 2013, *A&A*, 550, A61
- Lesur G., Kunz M. W., Fromang S., 2014, *A&A*, 566, A56
- Lesur G., Longaretti P.-Y., 2007, *MNRAS*, 378, 1471
- Lesur G., Ogilvie G. I., 2010, *MNRAS*, 404, L64
- Meyer F., Meyer-Hofmeister E., 1984, *A&A*, 132, 143
- Miller K. A., Stone J. M., 2000, *ApJ*, 534, 398
- Mineshige S., Osaki Y., 1983, *PASJ*, 35, 377
- Mineshige S., Wheeler J. C., 1989, *ApJ*, 343, 241
- Paczýński B., 1969, *Acta Astron.*, 19, 1
- Pessah M. E., Chan C.-k., Psaltis D., 2007, *ApJ*, 668, L51
- Potter W. J., Balbus S. A., 2014, *MNRAS*, 441, 681
- Sano T., Inutsuka S.-i., Turner N. J., Stone J. M., 2004, *ApJ*, 605, 321
- Sano T., Miyama S. M., Umebayashi T., Nakano T., 2000, *ApJ*, 543, 486
- Schreiber M. R., Hameury J.-M., Lasota J.-P., 2003, *A&A*, 410, 239
- Shakura N. I., Sunyaev R. A., 1973, *A&A*, 24, 337
- Shi J., Krolik J. H., Hirose S., 2010, *ApJ*, 708, 1716
- Shi J.-M., Stone J. M., Huang C. X., 2016, *MNRAS*, 456, 2273
- Simon J. B., Beckwith K., Armitage P. J., 2012, *MNRAS*, 422, 2685
- Smak J., 1984, *Acta Astron.*, 34, 161
- Smak J., 1999, *Acta Astron.*, 49, 391
- Sorathia K. A., Reynolds C. S., Armitage P. J., 2010, *ApJ*, 712, 1241
- Sorathia K. A., Reynolds C. S., Stone J. M., Beckwith K., 2012, *ApJ*, 749, 189
- Suzuki T. K., Inutsuka S.-i., 2009, *ApJ*, 691, L49
- Turner N. J., 2004, *ApJ*, 605, L45
- Turner N. J., Sano T., 2008, *ApJ*, 679, L131
- Turner N. J., Stone J. M., Krolik J. H., Sano T., 2003, *ApJ*, 593, 992
- van Paradijs J., 1996, *ApJ*, 464, L139
- Wardle M., 2007, *Ap&SS*, 311, 35

## APPENDIX A: NON-IDEAL MHD EFFECTS IN DWARF NOVA QUIESCENCE

Here we examine non-ideal MHD effects due to thermal ionization only (i.e. neglecting irradiation) and their possible importance in dwarf nova quiescence. By non-ideal MHD effects, we are referring to Ohmic dissipation (i.e. resistivity), the Hall term, and ambipolar diffusion. The full induction equation including these terms can be written as (Lesur

et al. 2014)<sup>13</sup>

$$\frac{\partial \mathbf{B}}{\partial t} - \nabla \times (\mathbf{v} \times \mathbf{B}) = -\frac{\nabla}{4\pi} \times (\eta_O \mathbf{J} + \eta_H \mathbf{J} \times \mathbf{e}_b - \eta_A \mathbf{J} \times \mathbf{e}_b \times \mathbf{e}_b), \quad (\text{A1})$$

where  $\mathbf{J} = 4\pi \nabla \times \mathbf{B}$  and  $\mathbf{e}_b = \mathbf{B}/|\mathbf{B}|$ . The terms on the right hand side are respectively the Ohmic resistive term (O), the Hall term (H), and the ambipolar diffusion term (A), where the  $\eta$  coefficients are the respective diffusivity coefficients. The Hall term is caused by a velocity difference between electrons (e) and heavy cations (i), while Ohmic dissipation and ambipolar diffusion are caused by collisions between neutrals (n) and electrons or cations respectively. Thus, it is worthwhile briefly discussing the relevant quantities involving these collisions. The momentum rate coefficients for ion-neutral and electron-neutral collisions are  $\langle \sigma v \rangle_{ni} = 1.9 \times 10^{-9} \text{ cm}^3 \text{ s}^{-1}$  (Draine 2011) and  $\langle \sigma v \rangle_{ne} = 8.3 \times 10^{-10} T^{1/2} \text{ cm}^3 \text{ s}^{-1}$  (Draine et al. 1983), respectively. The ion-neutral drag coefficient is therefore

$$\gamma = \frac{\langle \sigma v \rangle_{ni}}{m_n + m_i} = 2.7 \times 10^{13} \left( \frac{m_n + m_i}{41.37 m_u} \right)^{-1} \text{ cm}^3 \text{ s}^{-1} \text{ g}^{-1}, \quad (\text{A2})$$

where we have taken  $m_n = 2.37 m_u$  (the mean molecular weight for our abundances, taking all the hydrogen to be molecular), and  $m_i = 39 m_u$  ( $\text{K}^+$ , appropriate for thermal ionization; Balbus & Terquem 2001)<sup>14</sup>. The diffusivity coefficients for Ohmic, Hall, and ambipolar diffusion are as follows (in the absence of dust; Balbus & Terquem 2001; Wardle 2007; Lesur et al. 2014):

$$\eta_O = \frac{c^2 m_e n_n}{4\pi e^2 n_e} \langle \sigma v \rangle_{ne} \quad (\text{A3})$$

$$\eta_H = \frac{Bc}{4\pi e n_e} = \sqrt{\frac{\rho}{4\pi}} \frac{v_A c}{n_e e} \quad (\text{A4})$$

$$\eta_A = \frac{B^2}{4\pi \gamma_i \rho \rho_i} = \frac{v_A^2}{\gamma_i \rho_i}, \quad (\text{A5})$$

where  $v_A = B/\sqrt{4\pi\rho}$  is the Alfvén speed.

By introducing the isothermal sound speed  $c_s = \sqrt{kT/\mu m_u}$  we can examine the ratios

$$\frac{\eta_H}{\eta_O} = \sqrt{4\pi} \frac{v_A}{c_s} \sqrt{\frac{n_{\text{tot}}}{n_n}} \frac{\sqrt{kT}}{\langle \sigma v \rangle_{ne}} \frac{e}{cm_e} n_n^{-1/2} \quad (\text{A6})$$

$$= 1.14 \frac{v_A}{c_s} \sqrt{\frac{n_{\text{tot}}}{n_n}} \left( \frac{m_u n_n}{10^{-6} \text{ g cm}^{-3}} \right)^{-1/2}$$

$$\frac{\eta_A}{\eta_H} = \sqrt{4\pi} \frac{n_e}{n_i} \frac{v_A}{c_s} \frac{e}{\gamma_i c m_i \sqrt{\rho}} \sqrt{\frac{kT}{\mu m_u}} \quad (\text{A7})$$

$$= 6.61 \times 10^{-3} \frac{n_e}{n_i} \frac{v_A}{c_s} f_M (\rho_{-6})^{-1/2} \left( \frac{T}{3000 \text{ K}} \right)^{1/2}$$

$$f_M \equiv \left( \frac{m_i}{39 m_u} \right)^{-1} \left( \frac{m_n + m_i}{41.37 m_u} \right) \left( \frac{\mu}{2.37} \right)^{-1/2}, \quad (\text{A8})$$

where  $\rho_{-6} = \rho/10^{-6} \text{ g cm}^{-3}$ , and  $f_M = 1$  for the abundances

<sup>13</sup> Here we use Gaussian units, thus our presentation differs by factors of  $\sqrt{4\pi}$  compared to that of Lesur et al. (2014).

<sup>14</sup> Note that Blaes & Balbus (1994) adopted  $m_i = 30 m_u$ , appropriate for the interstellar medium; while Sano et al. (2000) adopted  $m_i = 24 m_u$  ( $\text{Mg}^+$ ) appropriate for ionization in accretion discs due to irradiation.

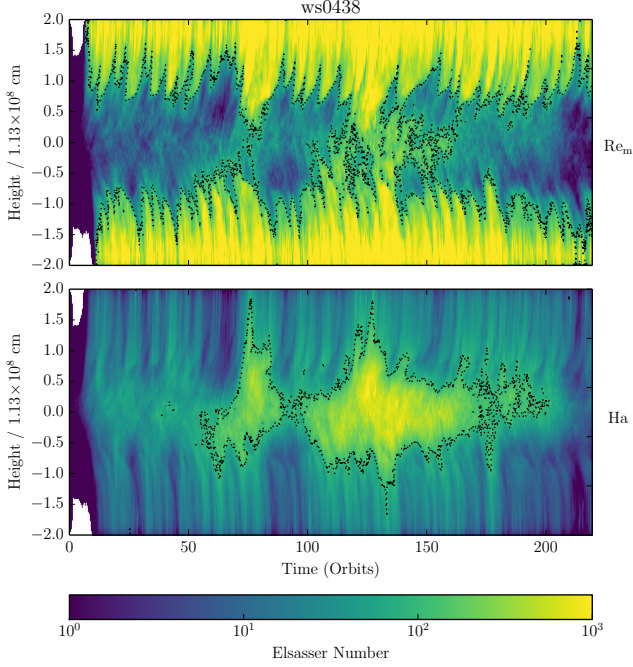


**Figure A1.** Horizontally averaged Elsasser numbers for the hottest lower branch simulation (ws0438). Lower Elsasser number corresponds to non-ideal MHD effects being more important.  $\text{Re}_m$  (Eq. A9, top panel) corresponds to Ohmic dissipation and  $\text{Ha}$  (Eq. A10, bottom panel) corresponds to the Hall term. Previous works (e.g. Hawley et al. 1996; Lesur & Longaretti 2007) suggest that Ohmic dissipation is important for  $\text{Re}_m \lesssim 100$ ; we have therefore plotted a dotted black contour at  $\text{Re}_m, \text{Ha} = 100$ . Non-ideal MHD effects are thus likely important for the majority of this simulation.

and masses we assume here. From this we immediately conclude that the Hall term will likely be important whenever the Ohmic dissipation is important, as we are typically talking about densities and temperatures in this range. However, ambipolar diffusion is negligible compared to both of the other two non-ideal effects.

To determine how important the Ohmic and Hall terms are, it is useful to examine the following dimensionless Elsasser numbers which can be computed from simulation profiles:

$$\text{Re}_m \equiv \frac{v_A^2}{\Omega \eta_O} \quad (\text{A9})$$

$$\text{Ha} \equiv \frac{v_A^2}{\Omega \eta_H} \quad (\text{A10})$$

For the hottest lower branch simulation (ws0438) we have computed the horizontally averaged Elsasser numbers (see Figure A1). Previous works (e.g. Hawley et al. 1996; Lesur & Longaretti 2007) show that Ohmic dissipation is important when  $\text{Re}_m$  is less than a few hundred and much of ws0438 has Elsasser numbers below 100 (the dotted black contour of Figure A1). The other lower branch simulations are colder than ws0438 and are therefore more susceptible to non-ideal effects, implying that non-ideal MHD effects are important in dwarf nova quiescence. Future work should therefore include Ohmic dissipation and the Hall term in

our simulations, but the ambipolar diffusion term is probably not necessary.

## APPENDIX B: SIMULATION PARAMETERS

The parameters for 3D MHD shearing-box simulations which appear in this paper but not in Hirose et al. (2014) are listed below in Table B1.

$T_{\text{eff}}$	$\Sigma$	$\alpha$	$\tau_{\text{tot}}$	$T_{\text{eff},0}$	$\Sigma_0$	$\alpha_0$	$\beta_0$	$h_0/10^8$	$N_x$	$N_y$	$N_z$	$L_x/h_0$	$L_y/h_0$	$L_z/h_0$	$L_z/h_P$	$t_{\text{th}}$	$t_{\text{max}}$
$R = 1.25 \times 10^9$ cm																	
8932	10.7	0.090	5876	8709	10.9	0.042	10	0.226	32	64	384	0.50	2.00	6.00	15.2	13.8	189
9427	12.2	0.068	4910	7943	12.5	0.026	10	0.210	32	64	384	0.50	2.00	6.00	11.5	17.1	114
9698	14.7	0.055	5162	7943	14.9	0.020	10	0.221	32	64	384	0.50	2.00	6.00	10.9	19.7	118
17405	85.8	0.037	6985	16218	86.4	0.026	100	0.447	32	64	512	0.50	2.00	6.00	13.4	24.4	133
19471	106	0.042	6798	16218	107	0.020	10	0.462	32	64	512	0.50	2.00	6.00	13.0	20.9	139
$R = 4.13 \times 10^9$ cm																	
7546	36.7	0.134	17221	8709	37.2	0.067	10	1.55	32	64	384	0.50	2.00	6.00	22.7	11.0	165
8079	40.4	0.099	16800	9549	40.6	0.081	10	1.71	32	64	384	0.50	2.00	6.00	19.9	12.8	114
8542	45.2	0.076	14139	9549	45.5	0.070	10	1.75	32	64	384	0.50	2.00	6.00	16.4	15.1	122
9324	52.0	0.069	9283	9549	52.5	0.058	10	1.80	32	64	384	0.50	2.00	6.00	13.9	15.9	123

**Table B1.** Parameters for simulation runs.  $T_{\text{eff}}$ ,  $\Sigma$ ,  $\alpha$ , and  $\tau_{\text{tot}}$  are the time averaged effective temperature in K, column mass density in  $\text{g cm}^{-2}$ , Shakura & Sunyaev (1973)  $\alpha$ -parameter, and optical depth respectively.  $T_{\text{eff},0}$ ,  $\Sigma_0$ ,  $\alpha_0$ , and  $\beta_0$  are the initial condition values where  $\beta_0$  is the initial ratio of gas to magnetic pressure.  $h_0/10^8$  is the simulation length unit over  $10^8$  cm.  $N_x$ ,  $N_y$ ,  $N_z$  are the number of grid cells in the  $x$ ,  $y$ , and  $z$  directions respectively.  $L_x/h_0$ ,  $L_y/h_0$ ,  $L_z/h_0$  are dimensions of the simulation domain in the  $x$ ,  $y$ , and  $z$  directions respectively.  $L_z/h_P$  is the height of the simulation domain over the time averaged pressure scale height.  $t_{\text{th}}$  is the time averaged thermal time.  $t_{\text{max}}$  is the maximum runtime used for time averaging.